Theoretical study of charge transport in Li-based batteries

Inaugural-Dissertation

to obtain the academic degree

Doctor rerum naturalium (Dr. rer. nat.)

submitted to the Department of Biology, Chemistry and Pharmacy

of Freie Universität Berlin

by

Ashkan Moradabadi

Berlin, 04.12.2017

This thesis was prepared under the supervison of Dr. Payam Kaghazchi at Freie Universität Berlin from March 2014 until March 2017.

The originality of this work is confirmed by the author.

Reviewer 1: Dr. Payam Kaghazchi
Reviewer 2: Prof. Dr. Beate Paulus

Freie Universität Berlin
Physikalische und Theoretische Chemie
Institut für Chemie und Biochemie

Date of defense: October 23th 2017

To Sareh

Abstract

The performance of Li-ion batteries is mainly determined by ionic and electronic conductivities of the electrode materials. Both transport properties were studied in this dissertation using *ab initio*-based calculations together with thermodynamic and kinetic analysis in three electrode materials. Here, the Li transport in Si as a future anode material as well as $LiCoO_2$ as the most commonly used and Li_2S as a promising cathode materials were investigated. Each of them shows a distinct Li diffusion mechanism and hence different ionic transport properties. In addition, effect of stress/strain on the ionic and electronic mobilities in bulk $LiCoO_2$ were evaluated within the theory of elasticity.

In the first section, lithiation of the crystalline silicon anode (c-Si), which results in the formation of a two-phase system consisting of amorphous Li_2Si (a-Li_2Si) as shell around c-Si as core, was investigated. The lithiation of silicon nanowires, which is accompanied by an anisotropic swelling, is governed by the motion of the interfaces between a-Li_2Si and c-Si. To reveal the origin of this phenomenon, adsorption and migration of Li were first evaluated at the three most stable surfaces of c-Si. It was shown that the adsorption of Li initially starts from the (110) surface with the lowest Li migration energy at the highest Li concentration. Afterwards, Li migration was estimated at three explicitly-modeled interfaces of a-Li_2Si/c-Si corresponding to the three surfaces of c-Si. It was found that the origin of the anisotropic swelling is not due to a faster ionic diffusion at the interfaces but it is because of thermodynamic reasons related to various interface stabilities. Thus, the growth process at the interfaces of a-Li_2Si/c-Si is orientation dependent. The a-Li_2Si/c-Si(110) interface has the highest formation energy, lowest stability and hence highest interface mobility among the others which is in agreement with experimental findings.

In the second section, thermodynamics and kinetics of defects in Li_2S cathode material were studied. To find the origin of the low ionic conductivity in Li_2S, the formation and migration of defects in this material were investigated. It was demonstrated that the Li diffusion in Li_2S is driven by the formation of Frenkel pairs and migration of single Li vacancies since migration of interstitials Li is not energetically favorable. The lithiation process in Li_2S is accompanied by a high activation energy. Therefore, since the formation energies for Li vacancy and interstitial are almost the same, the ionic conductivity is controlled by the kinetic, i.e. the migration energy of single Li vacancies.

For $LiCoO_2$ cathode material with a layered structure, first the mechanisms of Li migra-

tion both in bulk and on the $(10\bar{1}4)$ surface were investigated. It was shown that the planar lithiation in both bulk and $(10\bar{1}4)$ surface occurs via the diffusion of Li into a divacancy of Li on a curved pathway. This process, in the case of the topmost layer of $(10\bar{1}4)$ surface, takes place with no energy barrier. The lithiation process in $LiCoO_2$ is accompanied by hole-polaron hopping, which can only be detected using a DFT functional corrected with an onsite Hubbard term for Co, and as a result increases the migration energy of lithium. Estimated electronic conductivity in bulk $LiCoO_2$ is in good agreement with experimental value. Additionally, the effect of stress/strain on charge carriers mobilities was investigated in bulk $LiCoO_2$ by means of the "elastic dipole tensor (EDT)" method. Li diffusion energy barrier decreases with lateral tensile strain while the formation energy of Li vacancy increases, however, the effect of strain on the migration energy is stronger. 1% longitudinal strain in bulk $LiCoO_2$ can change the ionic conductivity more than one order of magnitude. The effect of stress/strain on electronic conductivity is opposite and less pronounced than that of the ionic one. The results obtained from the computationally efficient EDT method for both ionic and polaronic transports are in very good agreement with the conventional computationally-demanding method.

Zusammenfassung

Die Leistung von Li-Ionen-Batterien wird hauptsächlich durch ionische und elektronische Leitfähigkeiten der Elektrodenmaterialien bestimmt. Beide Transporteigenschaften wurden in dieser Dissertation mit ab initio-basierten Berechnungen zusammen mit thermodynamischen und kinetischen Analysen in drei Elektrodenmaterialien untersucht. Hier wurden den Li-Transport im Si als zukünftiges Anodenmaterial, $LiCoO_2$ als das am häufigsten verwendete und Li_2S als ein sehr vielversprechendes Kathodenmaterial untersucht. Jedes von ihnen zeigt einen anderen Li-Diffusionsmechanismus und damit unterschiedliche ionische Transporteigenschaften. Darüber hinaus wurde die Wirkung von Stress/Dehnung auf ionische und elektronische Mobilitäten in Bulk $LiCoO_2$ innerhalb der Theorie der Elastizität ausgewertet.

Im ersten Abschnitt wird die Lithiierung von einer kristallinen Silizium-Anode (c-Si) untersucht, die durch die Bildung eines Zweiphasensystems entsteht, mit amorphem Li_2Si (a-Li_2Si) als Hülle um c-Si als Kern. Die Lithiierung von Silizium-Nanodrähten, die begleitet wird von einer anisotropen Ausdehnung, erfolgt durch die Bewegung der Grenzflächen zwischen a-Li_2Si und c-Si. Um den Ursprung dieses Phänomens zu enthüllen, wurden zuerst Adsorption und Migration von Li an den drei stabilsten Oberflächen von c-Si ausgewertet. Es wurde gezeigt, dass die Adsorption von Li zunächst auf der (110) Oberfläche mit der niedrigsten Li-Migrationsanergie bei der höchsten Li-Konzentration beginnt. Danach wurde die Li-Migration für drei explizit modellierte Grenzflächen von a-Li_2Si/c-Si, die den drei Oberflächen von c-Si entsprechen, untersucht. Die Ergebnisse zeigten, dass der Ursprung der anisotropen Ausdehnung nicht auf eine schnellere ionische Diffusion an den Grenzflächen zurückzuführen ist, sondern auf thermodynamischen Gründen, die sich auf verschiedene Grenzflächenstabilitäten beziehen. Daher ist der Wachstumsprozess an den Schnittstellen von a-Li_2Si/c-Si orientierungsabhängig. Die a-Li_2Si/c-Si(110) Grenzfläche besitzt die höchste Grenzflächenbildungsenergie, die niedrigste Stabilität und damit die höchste Mobilität der untersuchten Grenzflächen, was mit dem Experiment übereinstimmt.

Im zweiten Abschnitt wurden die Thermodynamik und Kinetik von Defekten im Li_2S Kathodenmaterial untersucht. Um den Ursprung der niedrigen Ionenleitfähigkeit in Li_2S heraus zu finden, wurden die Defektbildung und -migration in diesem Material untersucht. Es wurde gezeigt, dass die Li-Diffusion in Li_2S durch die Bildung von Frenkel-Paaren und die Migration von einzelnen Li-Leerstellen angetrieben wird, da die Migration

von interstitiellen Li-Ionen energetisch nicht günstig ist. Der Lithiierungsprozess wird von einer hohen Aktivierungsenergiebarriere begleitet. Daher wurde gefolgert, dass, da die Formationsenergien für Li-Leerstellen und Interstitiale fast gleich sind, die Ionenleitfähigkeit wird durch kinetische gesteuert, und damit die Migrationsenergie einzelner Li-Leerstellen.

Für das $LiCoO_2$ Kathodenmaterial mit einer Schichtstruktur, wurden zunächst die Mechanismen der Li-Migration sowohl im Bulk als auch auf der $(10\bar{1}4)$ Oberfläche untersucht. Es wurde gezeigt, dass die planare Lithiierung sowohl im Bulk als auch der $(10\bar{1}4)$ Oberfläche über die Diffusion von Li in eine Divakanz von Li auf einem gekrümmten Weg erfolgt. Dieser Vorgang, im Falle der oberste Schicht der $(10\bar{1}4)$ Oberfläche, erfolgt ohne Energiebarriere. Der Lithiierungsprozess in $LiCoO_2$ wird von einem Loch-Polaron-Hopping begleitet, das nur mit einem DFT-Funktional erkannt werden kann, das mit einem lokalen-Hubbard-Term für Co korrigiert wird und die Migrationsenergie von Lithium erhöht. Die berechnete elektronische Leitfähigkeit in Bulk $LiCoO_2$ ist in sehr guter Übereinstimmung mit dem experimentellem Wert. Darüber hinaus wurde die Wirkung von Stress/Dehnung auf Ladungsträger-Mobilitäten mittels des "elastischen Dipol-Tensors (EDT)" Verfahrens in Bulk $LiCoO_2$ untersucht. Die Li-Diffusionsenergiebarriere nimmt mit lateraler Zugbeanspruchung ab, während die Vakanz-Bildungsenergie zunimmt, jedoch ist der Effekt der Dehnung auf die Migrationsenergie stärker. 1% Längsdehnung in Bulk $LiCoO_2$ kann die Ionenleitfähigkeit mehr als eine Größenordnung verändern. Dieser Effekt ist gegenüber und weniger ausgeprägt im Fall der elektronischen Leitfähigkeit. Die Ergebnisse aus dem rechnerisch effizienten EDT Verfahren stimmen sowohl für ionische als auch polaronische Transporte mit dem konventionellen rechnerisch anspruchsvollen Verfahren ausgezeichnet überein.

Contents

List of Publications

A1:

"On the origin of anisotropic lithiation of silicon"

Jochen Rohrer, Ashkan Moradabadi, Karsten Albe, Payam Kaghazchi

Journal of Power Sources 293 (2015), pp. 221-227.

DOI: 10.1016/j.jpowsour.2015.05.057

A2:

"Thermodynamics and kinetics of defects in Li_2S"

Ashkan Moradabadi and Payam Kaghazchi

Applied Physics Letters 108 (2016), p. 213906.

DOI: 10.1063/1.4952434

A3:

"Mechanism of Li intercalation/deintercalation into/from the surface of $LiCoO_2$"

Ashkan Moradabadi and Payam Kaghazchi

Physical Chemistry Chemical Physics 17 (2015), pp. 22917-22922.

DOI: 10.1039/c5cp02246k

A4:

"Influence of elastic strain on the thermodynamics and kinetics of lithium vacancy in bulk $LiCoO_2$"

Ashkan Moradabadi, Payam Kaghazchi, Jochen Rohrer and Karsten Albe

Submitted to *Physical Review Materials*, June 2017, Requested for minor revision

URL: https://arxiv.org/abs/1706.01709

A5:

"Effect of strain on polaron hopping and electronic conductivity in bulk $LiCoO_2$"

Ashkan Moradabadi, Payam Kaghazchi

Physical Review Applied 7 (2017), p. 064008.

DOI: 10.1103/PhysRevApplied.7.064008

Additional Publications

D1:

"Effect of anode composition on solid electrolyte interphase formation"
Ashkan Moradabadi, Maryam Bakhtiari and Payam Kaghazchi
Electrochimica Acta 213 (2016), pp. 8-13
DOI: 10.1016/j.electacta.2016.07.042

D2:

"Structure and ionic conductivity of the solid electrolyte interphase layer on tin anodes in Na-ion batteries"
Liang-Yin Kuo, Ashkan Moradabadi, Hsin-Fu Huang, Bing-Joe Hwang and Payam Kaghazchi
Journal of Power Sources 341 (2017), pp. 107-113
DOI: 10.1016/j.jpowsour.2016.11.077

D3:

"Evidence of a strong effect of defect-free metal oxide supports on Pt nanoparticles"
Ashkan Moradabadi, Shideh Ahmadi and Payam Kaghazchi
Nanoscale 9 (2017), pp. 4478-4485
DOI: 10.1039/c6nr07816h

D4:

"Elucidating the origin of HER activity in mono- and bimetallic metal- and nitrogen-doped carbon catalysts (Me-N-C)"
Ali Shahraei, Ashkan Moradabadi, Ioanna Martinaiou, Stefan Lauterbach, Sebastian Klemenz, Stephanie Dolique, Hans-Joachim Kleebe, Payam Kaghazchi and Ulrike Kramm
Applied Materials and Interfaces 9 (2017), pp. 25184–25193
DOI: 10.1021/acsami.7b01647

List of Abbreviations

LIB	Li-ion batteries
LCO	$LiCoO_2$
2D, 3D	Two-, Three-dimension(al)
SEI	Solid Electrolyte Interphase
DFT	Density Functional Theory
XC	Exchange-Correlation Functional
LDA	Local Density Approximation
GGA	General gradient approximation
LCAO	Linear combination of atomic orbitals
PBE	Perdew-Burke-Ernzerhof (PBE functional)
EDT	Elastic Dipole Tensor
FNV	Freysoldt, Neugebauer and Van de Walle (Energy Correction Method)
NEB	Nudge Elastic Band
Cl-NEB	Climbing Nudge Elastic Band
TST	Transition State Theory
PES	Potential Energy Surface

List of Figures

1 Introduction

In "electrochemistry" conversion between chemical and electrical energies is studied [1, 2]. The chemical reactions, i.e. oxidation and reduction also referred to as "redox" reactions, occur as a result of ionic and electronic charge transfers between atomic or molecular species which lead to a change in their oxidation states [1, 2]. Therefore, electronic and ionic conductivities play important roles in electrochemistry [3]. Ionic conductivity in battery materials occurs via the movements of ions. These movements can be either in the form of single hopping or cooperative (synchronized) motions (see section 2.2). Electronic conductivity in battery materials is governed by electron (or hole) transport which mainly takes place via polaron-hopping (see section 2.4) [4, 5, 6].
In rechargeable Li-ion batteries (LIB) which are one of the main branches in electrochemistry, charging and discharging processes can be performed repeatedly up to 1000 cycles [7, 8, 9]. Li-ion (Fig. 1) and Li-S (Fig. 2-a) batteries (both are referred to as LIB) are among the most promising rechargeable energy storage devices [10, 11].
In this thesis, the focus is on the transport properties in some electrode materials of rechargeable LIB where the migration of lithium ions (or vacancies) as well as electrons (or holes), both as the charge carriers, are decisive [3]. The aim is to study the transport properties with different mechanisms using quantum mechanical atomistic modeling and to investigate the approaches by which the transport phenomena in LIB may be modified.

1.1 Working principles of Li-ion and Li-S batteries

Li-ion batteries

Fig. 1 shows the schematic of a commercially used Li-ion battery cell, consisting of an anode (e.g. carbon in the form of graphite), an electrolyte (e.g. diethyl carbonate, i.e. DEC, and salts such as $LiPF_6$) and cathode (e.g. $LiCoO_2$). **Anode** is the negative electrode, where during the charging process, reduction of Li^+ ions coming from the electrolyte by collecting the electrons occur. **Cathode** is the positive electrode where the oxidation of its material (e.g. $LiCoO_2$ in the case of Fig. 1) and releasing the electrons take place. The working mechanism of a typical Li-ion cell is as the following steps. During the charging process, Li ions are extracted (deintercalated) from the cathode material ($LiCoO_2$) via electrochemical oxidation process. By passing through the electrolyte, Li ions are inserted (intercalated) into the graphite anode which is accompanied by electrochemical reduction process [7]. Both graphite anode and $LiCoO_2$ cathode have layered structures which are

suitable for Li storage [12]. The processes for discharging on both sides are the opposite of charging. Following reactions summarize the charging processes in a typical Li-ion battery (see Fig. 1):

$$\text{(Cathode)} \qquad \mathrm{Li_xMO_2} \longrightarrow \mathrm{yLi^+ + y\,e^- + Li_{x-y}MO_2} \tag{1}$$

$$\text{(Anode)} \qquad \mathrm{y\,Li^+ + y\,e^- + C_6} \longrightarrow \mathrm{Li_yC_6} \tag{2}$$

$$\text{(Overall)} \qquad \mathrm{C_6 + Li_xMO_2} \longrightarrow \mathrm{Li_yC_6 + Li_{x-y}MO_2} \tag{3}$$

Electrodes in LIB are separated via the **electrolyte** which is an inert material and must stay stable within a certain temperature range [13]. Typically, the liquid electrolytes are composed of an organic liquid media (e.g. DEC) together with dissoluble Li-contained salts. The **solid electrolyte interphase (SEI)**, which is a heterostructure layer, forms on both electrodes (mainly on the anode) as a result of the chemical decomposition of electrolyte during first cycles of charging and discharging. The formation of a SEI is essential in LIB since this layer prevents further decomposition of electrodes by partially blocking the electron transport [14, 15]. Due to the nature of its structure, the ionic conductivity of the SEI layer is typically low. Since in this thesis the electrolyte part is not the subject of the studies, hence, a detailed discussion of electrolyte and the SEI is not provided.

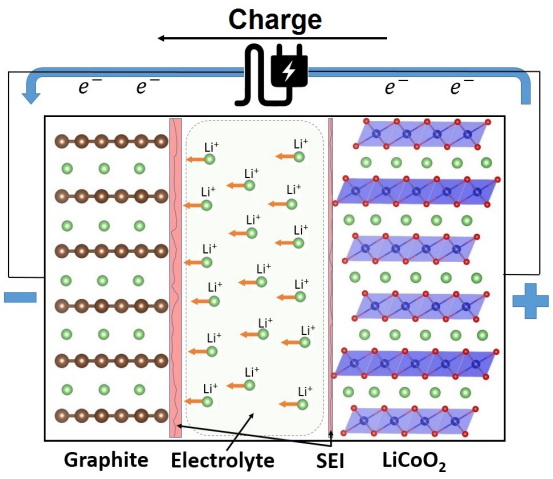

Figure 1: Schematic of a commercially used Li-ion battery. C, Li, Co and O atoms are shown with brown, light green, blue and red colors, respectively.

Li-S batteries

There have been significant progresses in Li-S batteries, a type of LIB which offers large specific capacity, low production cost and environmentally-friendly features [10, 16]. Usually in this type of batteries, the materials for anode and cathode are metallic Li and sulfur (S_8) (or its combination with carbon), respectively, as shown in Fig. 2-a. Recently, direct use of Li_2S as cathode together with a Li-free anode (e.g. silicon) has increasingly received attentions [16, 17, 18]. The advantage of the latter is related to the large theoretical capacity of Li_2S (1166 $mAhg^{-1}$) which potentially makes it an excellent cathode material [16]. The second reason is the fact that Li-free anodes do not suffer from the formation

of dendrites which is a common problem in Li and Li-based anodes [16, 17]. In batteries with S_8 cathode, formation of Li_2S crust around the S_8 core or Li_2S clusters as the final product of the lithiation process has been reported (see Fig. 2-b) [19, 20]. Due to the low ionic and electronic conductivity in Li_2S and also the shuttle effect (formation and diffusion of soluble polysulfides, i.e. Li_2S_8, Li_2S_6, Li_2S_4 and Li_2S_2, through the electrolyte into the anode), the commercialization of Li-S batteries is still a challenge. However, it has been proposed that using nanosized Li_2S or mixed compositions of Li_2S with carbon-based materials as the cathode can greatly overcome the issue of low conductivity in Li_2S [16, 18, 21].

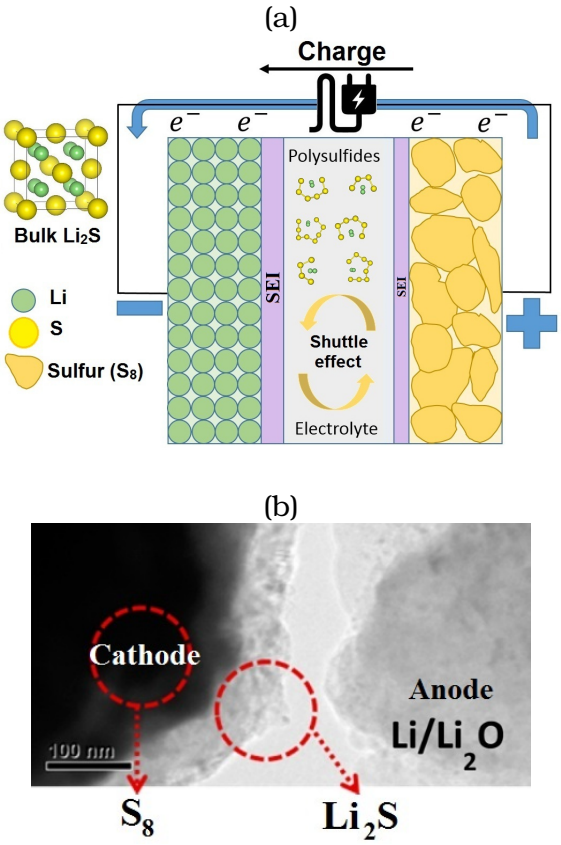

Figure 2: (a) Schematic of Li-S battery with sulfur cathode as well as the crystal structure of Li_2S. (b) TEM image from the reference [19] of a Li-S cell during the discharge process. Formation of Li_2S as a shell around S_8 as a core is evident.

One of the differences between Li-S and Li-ion batteries is the distinct Li diffusion mechanisms in the electrodes. In Li-S batteries with Si anode and Li_2S cathode, three-dimensional (3D) Li diffusion together with the formation of a new phase in the anode and 3D diffusion of Li ions in single Li vacancies without any chemical reaction (for low defects concentration) in the cathode are the dominant processes for the ionic transport [10, 16, 18, 22, 23]. On the other hand, in Li-ion batteries with $LiCoO_2$ cathode, 2D diffusion of Li ions in Li divacancies takes place in such a way that Li ions (or vacancies) move laterally between octahedral planes of O-Co-O [11, 12, 24]. In the following sections, charge transport phenomena during the lithiation/delithiation processes in some electrode materials are discussed. The selected materials are Si and Li_2S as promising candidates for anode and cathode in Li-S batteries, respectively, as well as $LiCoO_2$ as the most widely used cathode material in Li-ion batteries. Mechanisms of Li diffusion and the key factors in the transport phenomenon, i.e. thermodynamics or kinetics, in each case are different.

1.2 Anode materials

1.2.1 Si anode

In the current generation of LIB, carbon in the form of graphite is used as the common anode material. The structure of graphite consists of carbon atoms in a hexagon form which are linked in a layer by layer fashion [25]. As a result, graphite has the potential to store Li ions within its layered structure. In spite of various advantages of graphite as anode material, such as large reversible capacity and good mechanical stability during the lithiation/delithiation processes [27, 28, 29], due to its very low theoretical capacity of 372 $mAhg^{-1}$, there have been many efforts to find its replacements. Recently, silicon (Si) has been introduced as a promising anode material with a theoretical capacity of $\sim$4140 $mAhg^{-1}$, which is more than 10 times larger than that of graphite [30]. In contrast to graphite, lithiation process in crystalline silicon (c-Si) takes place in 3D and is accompanied by chemical reactions leading to the formation of amorphous Li_2Si (a-Li_2Si) phase [23]. Due to the poor cyclability and irreversible capacity fading, which are mainly related to the large lattice expansion and volume changes during the lithiation/delithiation processes (up to $\sim$ 300 %), silicon as anode has not been commercialized yet [31]. It has been reported that using silicon nanostructures or mixed compounds of carbon and silicon can significantly rectify this problem [30, 32]. Further studies also indicated that during the lithiation process in silicon nanowires, by formation of the two-phase system of a-Li_2Si/c-Si, an anisotropic swelling appears which is more significant along the <110> direction (see Fig. 3) [26, 33, 34]. In fact, the growth process is controlled by the movements of the interfaces between a-Li_2Si and c-Si. The origin of this peculiar volume change, which can eventually lead to the fracture of silicon nanowires, is not well understood. In this thesis, using density functional theory calculations, the lithiation at the three most stable surfaces of c-Si as the first cycle of lithiation is studied. Furthermore, by creating a realistic two-phase model with c-Si as core and a-Li_2Si as shell, the thermodynamic and kinetic of the lithiation process at the interfaces of a-Li_2Si/c-Si are evaluated (see publication **A1**) [35].

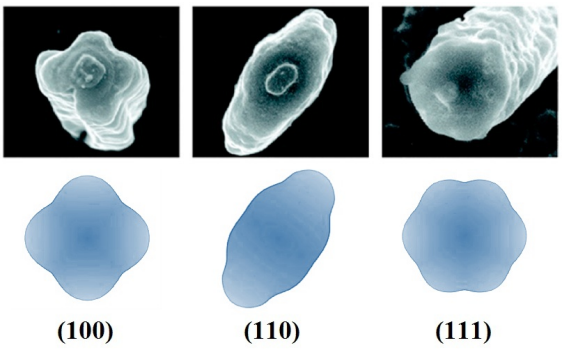

Figure 3: Top: SEM images from reference [26] of fully lithiated silicon nanowires which show the orientation-dependent anisotropic swelling. Bottom: Schematic of anisotropic expansion along three different orientations.

1.3 Cathode materials

1.3.1 Li_2S cathode

As mentioned earlier, Li_2S as an important specie in Li-S batteries, i.e. either directly used as cathode material or created as a by-product, has a very low ionic and electronic conductivity [17]. Since there is limited knowledge on the transport properties of Li_2S, in the second section of the results chapter, defect chemistry, i.e. thermodynamic and kinetic of defects, as well as various Li diffusion mechanisms in Li_2S are studied using density functional theory calculations (see publication **A2**) [22]. In this study, calculated defect formation energy ($\Delta E_{\mathrm{F}}^{i,q}$) as function of chemical potential of Li (μ_{Li}) for all possible defect types is plotted. Using this plot, the most energetically favorable defect type in Li_2S at various cell voltages can be predicted. Moreover, Li diffusion energy barriers for single and divacancy as well as knock-off interstitial mechanisms are computed. Finally, the activation energy for the Li transport in bulk-Li_2S is estimated which is then used by my colleagues in another study [36] to estimate the ionic conductivity by means of Nernst-Einstein and Arrhenius type relationships presented by Eqs. 2.2.1 and 2.2.2 in section 2.2.

1.3.2 $LiCoO_2$ cathode

$LiCoO_2$ (LCO) was first proposed by Mizushima *et al.* [37] for the cathode application. LCO with the $R\bar{3}m$ space group and a theoretical capacity of ~ 274 mAhg^{-1} [38] consists of $CoO_2{}^{-2}$ octahedrals arranged in layers with Co in the center and Li ions located between these layers (see Fig. 1). To improve the rate of charging/discharging processes in LCO, nanosizing as a promising approach has been proposed [39]. The reason of this effect can be explained by shorter diffusion length for Li ions as a result of nanosizing which increases the charging/discharging rates [39]. On the other hand, weaker bonding between topmost Co and O on the surface of LCO nanoparticles can decrease the energy barrier for Li intercalation/deintercalation at the topmost surface layer [24]. In the present thesis, the mechanisms of Li diffusion in bulk and one of the most stable surfaces, i.e. $(10\bar{1}4)$, of LCO are studied. In addition, effect of magnetic and non-magnetic defects states as well as using PBE and PBE+U functionals on the Li migration in both bulk and $(10\bar{1}4)$ surface are investigated (see publication **A3**) [24].

1.4 Effect of stress on ionic and electronic conductivity

One of the important factors that can affect the conductivity (ionic, electronic or even thermal) is stress/strain fields [40, 41, 42, 43]. The stress/strain in batteries can originate from various sources. For example, it can be applied externally during the packing of a battery cell. It may also be generated in bulk of materials as a result of the lithiation/delithiation processes or in general from the chemical reactions. In this case, phase transition and formation of a two-phase system within the bulk, similar to the lithiation of silicon anode, leads to changes in the lattice parameters of the structures. Consequently, stress/strain due to lattice mismatches between different phases may appear. The stress/strain can also appears on surfaces or at interfaces. For instance, in batteries with solid electrolyte, again due to lattice mismatches between electrodes and solid electrolyte, interfacial stress/strain can be observed. Another example can be the interfacial stress/strain between electrodes and SEI in the case of batteries with liquid electrolyte [44, 45, 46, 47]. Therefore, investigation of the effect of stress/strain on ionic mobility in LIB is imperative. In the third section of the results chapter, the effect of stress/strain on the ionic conductivity in $LiCoO_2$ using the "**elastic dipole tensor (EDT)**" method (section 2.3.2) is discussed [48]. In this study, finite unit cell size effect on the calculation of elastic dipole tensor (G_{ij}) is investigated. Moreover, it is aimed at showing that the results obtained from the computationally efficient EDT method can be in agreement with the conventional computationally-demanding approach where the conductivity as a function of strain should be computed at each strain regime separately. (see publication **A4**).

A wide variety of the materials that are used as electrodes in LIB are semiconductors. In highly polar semiconductors, due to the interactions between extra electrons (or holes) and positive (or negative) ions in a crystal "virtual phonons" are created and the overall sets form quasiparticles referred to as **"polarons"**. Since the formation of a polaron is energetically favorable, it is occurred spontaneously and thus is referred to as a "**self-trapped"** condition [49, 50]. By means of the transition state theory and in case of adiabatic electron transfer, it is possible to calculate the energy barrier and hence the electronic conductivity for the migration of an electron- (or hole-) polaron [49]. In the last section, the electronic conductivity in the case of bulk $LiCoO_2$ is calculated using the concept of small hole-polaron hopping. Moreover, the effect of stress/strain on the electronic conductivity is evaluated using both the direct and the EDT methods (see publication **A5**) [51].

2 Theory

2.1 Quantum Mechanical Calculation Methods

Following by the efforts of Thomas, Fermi and Dirac in expressing the total energy of a many body system as a functional of its electron density, density functional theory (DFT) was introduced by P. Hohenberg and W. Kohn [52] and afterwards developed further by W. Kohn and L.J. Sham [53]. This theory enables us to predict the ground state energy (and hence other ground state properties) of a system as a functional of its electron density ($\rho(\vec{r})$). In the following sections, the many body problem including important wave function as well as electron density based approaches for the calculation of ground state energy in a system of atoms or molecules will be explained.

2.1.1 Schrödinger Equation

The total energy of a system can be calculated by means of the Schrödinger equation which in its time-independent and non-relativistic form can be written as [54, 55]:

$$\hat{H}\Psi_i(\vec{r}_1, \vec{r}_2, ..., \vec{r}_{\mathrm{n}}, \vec{R}_1, \vec{R}_2, ..., \vec{R}_{\mathrm{m}}) = E_i\Psi_i(\vec{r}_1, \vec{r}_2, ..., \vec{r}_{\mathrm{n}}, \vec{R}_1, \vec{R}_2, ..., \vec{R}_{\mathrm{m}}). \tag{2.1.1}$$

In this eigenvalue equation, $\hat{H}$ is the Hamiltonian operator for any atomic and/or molecular system consisting of *n* electrons and *m* nuclei, $\vec{r}_{\mathrm{n}}$ and $\vec{R}_{\mathrm{m}}$ represent coordinates of electron and nuclei, respectively, Ψ_i is the overall wave function of the system and E_i are the energy eigenvalues, which results from the Hamiltonian operator acting on the wave function of the system. Practically, calculating the *exact* wave function of a system is not feasible, however, using high level quantum chemistry approaches for small systems, obtaining a very good (almost exact) approximation of the wave function is possible. The above-mentioned Hamiltonian can be written in atomic unit as the following expression:

$$\hat{H} = \underbrace{-\frac{1}{2}\sum_{i=1}^{\mathrm{n}}\nabla_i^2}_{T_{\mathrm{e}}} \underbrace{-\frac{1}{2}\sum_{\mathrm{A}=1}^{\mathrm{m}}\frac{1}{m_{\mathrm{A}}}\nabla_{\mathrm{A}}^2}_{T_{\mathrm{nu}}} \underbrace{-\sum_{i=1}^{\mathrm{n}}\sum_{\mathrm{A}=1}^{\mathrm{m}}\frac{Z_{\mathrm{A}}}{r_{i\mathrm{A}}}}_{V_{\mathrm{e-nu}}} + \underbrace{\sum_{i=1}^{\mathrm{n}}\sum_{j>i}^{\mathrm{n}}\frac{1}{r_{ij}}}_{V_{\mathrm{e-e}}} + \underbrace{\sum_{\mathrm{A}=1}^{\mathrm{m}}\sum_{\mathrm{B}>\mathrm{A}}^{\mathrm{m}}\frac{Z_{\mathrm{A}}Z_{\mathrm{B}}}{r_{\mathrm{AB}}}}_{V_{\mathrm{nu-nu}}}. \tag{2.1.2}$$

In the above Hamiltonian, m_{A}, Z_{A}, $r_{i\mathrm{A}}$, r_{ij} and r_{AB} are the mass of nuclei, atomic number, distance between electron-nuclei, distance between electron-electron and distance between nuclei-nuclei, respectively. T and V stand for the kinetic and potential energies, respectively. “e” and “nu” subscripts refer to electrons and nuclei, respectively.

2.1.2 Born-Oppenheimer Approximation

In order to simplify the general Hamiltonian in Eq. 2.1.2, the following assumption is considered. Since the mass of nucleus is in general much larger than that of electron (e.g. $m_A \approx 1{,}800$ for hydrogen and $m_A \approx 20{,}000$ for carbon), the movement of nuclei in an atom is much slower than that of electrons. As a result, in order to simplify the Hamiltonian of Eq. 2.1.2, Born and Oppenheimer suggested [56] that the electrons motions can be considered in the field of static nuclei. In fact, by semi-separating (not an exact separating) of variables, we can assume that the total wave function of $\Psi_i(\vec{r}_n, \vec{R}_m)$ is approximately equal to the product of nuclear and electronic wave functions, which leads to the decoupling of the total wave function into two parts. This approach is referred to as the **Born-Oppenheimer approximation**. Therefore, the general form of the total wave function for any system of atoms and molecules can be expressed as:

$$\Psi_i(\vec{r}_n, \vec{R}_m) = \psi_{elec}(\vec{r}_n; \vec{R}_m)\psi_{nuc}(\vec{R}_m). \tag{2.1.3}$$

In this equation, $\psi_{elec}(\vec{r}_n; \vec{R}_m)$ is the electronic part including the static electron-nuclei interactions and $\psi_{nuc}(\vec{R}_m)$ is the pure nuclei part. The general Hamiltonian of Eq. 2.1.2 for the electronic part can then be written as the following expression:

$$\hat{H}_{elec} = -\frac{1}{2}\sum_{i=1}^{n}\nabla_i^2 - \sum_{i=1}^{n}\sum_{A=1}^{m}\frac{Z_A}{r_{iA}} + \sum_{i=1}^{n}\sum_{j>i}^{n}\frac{1}{r_{ij}}, \tag{2.1.4}$$

where $\hat{H}_{elec}$ is the electronic Hamiltonian. Thus, by operating $\hat{H}_{elec}$ on the system, E_{elec} will be obtained as:

$$\hat{H}_{elec}\psi_{elec}(\vec{r}_n; \vec{R}_m) = E_{elec}(\vec{R}_m)\psi_{elec}(\vec{r}_n; \vec{R}_m), \tag{2.1.5}$$

The electronic energy term obtained from the Eq. 2.1.5 has a contribution to the motion of nuclei as:

$$\hat{H}_{nuc}\psi_{nuc}(\vec{R}_m) = \left\{ -\frac{1}{2}\sum_{A=1}^{m}\frac{1}{m_A}\nabla_A^2 + E_{elec}(\vec{R}_m) + \sum_{A=1}^{m}\sum_{B>A}^{m}\frac{Z_A Z_B}{r_{AB}} \right\}\psi_{nuc}(\vec{R}_m) = E_{tot}\psi_{nuc}(\vec{R}_m). \tag{2.1.6}$$

Hence, the total energy of the system (E_{tot}) can be calculated using Eq. 2.1.6. The imperative task is then to solve Eq. 2.1.5 and afterwards, using the Born-Oppenheimer approximation, the nuclei parts can be added to the total energy of the electronic part as parameter.

2.1.3 Hartree-Fock approximation

In order to construct a reasonable eigenstate (wave function of the n-electron system), Hartree proposed to use a simple approximation which consists of the multiplication of

n orthogonal spin orbitals χ (Hartree product [57]) as:

$$\Psi(\vec{r}_1, m_s; \vec{r}_2, m_s; ...; \vec{r}_{\rm n}, m_s) \approx \Psi_{\rm HP} = \chi(\vec{r}_1, m_s)\chi(\vec{r}_2, m_s)...\chi(\vec{r}_{\rm n}, m_s). \tag{2.1.7}$$

In this formula, $\chi(\vec{r}, m_s)$ consists of a spatial orbital ($\phi(\vec{r})$) and one spin function ($\sigma(s)$ which could be $\alpha(s)$ or $\beta(s)$, denoted by m_s). However, since this approximation does not satisfy the Pauli exclusion principle, i.e. antisymmetry principle, it is not physically logical. Later for the initial wave function, Slater proposed a physically meaningful antisymmetric wave function which is known as the **Slater determinant** [58] and can be expressed as:

$$\Psi(\vec{r}_1, m_s; \vec{r}_2, m_s; ...; \vec{r}_{\rm n}, m_s) \approx \Phi_{\rm SD} = \frac{1}{\sqrt{n!}} \begin{vmatrix} \chi_i(\vec{r}_1, m_s) & \chi_j(\vec{r}_1, m_s) & \dots & \chi_{\rm k}(\vec{r}_1, m_s) \\ \chi_i(\vec{r}_2, m_s) & \chi_j(\vec{r}_2, m_s) & \dots & \chi_{\rm k}(\vec{r}_2, m_s) \\ \vdots & \vdots & \ddots & \vdots \\ \chi_i(\vec{r}_{\rm n}, m_s) & \chi_j(\vec{r}_{\rm n}, m_s) & \dots & \chi_{\rm k}(\vec{r}_{\rm n}, m_s) \end{vmatrix} \tag{2.1.8}$$

In $\Phi_{\rm SD}$, the exact wave function of all **n** interacting electrons are replaced by **n** one-electron spin orbitals in which they only feel a Coulomb repulsive potential resulted from the average positions of other electrons. Moreover, there exists a non-classical concept of *exchange* which is resulted from the antisymmetric nature of $\Phi_{\rm SD}$. Since no electron-electron correlation is defined in this model, it is also referred to as a *mean field approach* as each electron interacts with an effective potential from all other electrons in the system.

Using the **"variational principle"** the best approximation of the true eigenstate corresponding (within the given ansatz) to the minimum energy eigenvalue can be calculated. According to this method, any suggested eigenstates ($\Psi_{\rm trial}$) will be an upper bound corresponding to the eigenvalues of the ground state energy which can be shown by the following relationship:

$$\langle \Psi_{\rm trial} | \hat{H} | \Psi_{\rm trial} \rangle = E_{\rm trial} \geq E_0 = \langle \Psi_0 | \hat{H} | \Psi_0 \rangle \,, \tag{2.1.9}$$

with Ψ_0 and E_0 as the exact wave function and the minimum energy of the system, respectively. In other words, to find the closest answer to the true eigenvalue (minimum energy of the system, E_0), Eq. 2.1.9 should be solved starting with a reasonably suggested eigenstate ($\Psi_{\rm trial}$, which will be explained in section 2.1.12) and keep being solved iteratively until a certain convergence criterion is fulfilled. The reasonably suggested eigenstates is referred to a selection from all possible eigenstates, with certain criteria such as to be continuous in space and to be quadratic integrable, by the use of which, $E_{\rm trial}$ within the variational method could become as close as possible to its minimum value. Therefore,

using Eq. 2.1.9, it is feasible to find the best approximation to the true ground state eigenstate (Ψ_0) and then the minimum energy of the system (E_0) can be determined.

In order to explain the Hartree-Fock method, the concept of the **Fock** ($\hat{F}$) operator [59, 60] is elaborated. $\hat{F}$ is an effective one-electron operator which acts on the $\chi_i(\vec{r}_{\rm n}, m_s)$ used in the Slater determinant as:

$$\hat{F}|\chi_i(\vec{r}_{\rm n}, m_s)\rangle = \epsilon_i|\chi_i(\vec{r}_{\rm n}, m_s)\rangle. \tag{2.1.10}$$

In this equation, the Fock operator is defined as:

$$\hat{F} = h_{1\rm e} + \underbrace{\sum_{\rm j\neq i}(\hat{J}_{\rm j} - \hat{K}_{\rm j})}_{V_{\rm HF}} = -\frac{1}{2}\nabla^2 - \sum_{\rm A}\frac{Z_{\rm A}}{r_{1\rm A}} + \underbrace{\sum_{\rm j\neq i}(\hat{J}_{\rm j} - \hat{K}_{\rm j})}_{V_{\rm HF}}, \tag{2.1.11}$$

where the first term ($h_{1\rm e}$) refers to the kinetic energy of one electron and the potential energy from the interaction of that electron with all nuclei. The last term ($V_{\rm HF}$) deals with the interaction of one electron with the other electrons (mean field interaction). In the $V_{\rm HF}$ expression, the first term is referring to the operator for *classical Coulomb* interaction between electrons. This concept for electron a between two electrons a and b in orbitals i and j, respectively, can be written by the following notation:

$$\begin{aligned} \hat{J}_{\rm ij} &= \langle ij|ij\rangle \\ \hat{J}_{\rm j}(a)\chi_i(\vec{r}_a, m_s) &= \left[\int d\vec{r}_b \chi_j^*(\vec{r}_b, m_s)\frac{1}{r_{ab}}\chi_j(\vec{r}_b, m_s)\right]\chi_i(\vec{r}_a, m_s). \end{aligned} \tag{2.1.12}$$

The second term of the Hartree-Fock potential is the *exchange* integral with a non-classical nature and can be written via the following notation:

$$\begin{aligned} \hat{K}_{\rm ij} &= \langle ij|ji\rangle \\ \hat{K}_j(a)\chi_i(\vec{r}_a, m_s) &= \left[\int d\vec{r}_b \chi_j^*(\vec{r}_b, m_s)\frac{1}{r_{ab}}\chi_i(\vec{r}_b, m_s)\right]\chi_j(\vec{r}_a, m_s). \end{aligned} \tag{2.1.13}$$

It should be noted that if electrons a and b would have antiparallel spin, since the spin orbitals become orthogonal, the exchange integral becomes zero.

By referring to Eq. 2.1.10, the orbital eigenenergies for the **n** electron system can be written as:

$$\epsilon_i = \langle\chi_i|\hat{F}|\chi_i\rangle = \langle\chi_i|\hat{h}_{1\rm e}(i)|\chi_i\rangle + \sum_j\langle\chi_i|\hat{J}_j|\chi_{\rm i}\rangle - \sum_j\langle\chi_i|\hat{K}_j|\chi_i\rangle. \tag{2.1.14}$$

Finally, the total energy of the electronic part (E_0) in terms of the eigenenergies can be expressed as:

$$E_0 = \sum_i^{\rm n}\epsilon_i - \frac{1}{2}\left(\sum_{i,j}\langle\chi_i|\hat{J}_j|\chi_i\rangle - \sum_{i,j}\langle\chi_i|\hat{K}_j|\chi_i\rangle\right). \tag{2.1.15}$$

It is shown that the Hartree-Fock method [59, 60] is a wave function-based approach in which the orthonormal single-particle spin orbitals in the form of Slater determinant is treated as the total wavefunction. Since in the Slater determinant the Pauli principle is considered, the exchange interaction of electrons with the same spins within the Hartree-Fock scheme is included. However, due to the fact that the correlation interactions for electrons with opposite spins is disregarded, E_{HF} is always larger than the exact total energy. The popular methods in the framework of wave function-based approaches for taking the correlation effects into account are configuration interaction (CI) [61], coupled cluster (CC) [62] and perturbation theory (MP2 and MP4) [63, 64, 65].

2.1.4 Density Functional Theory

In density functional theory (DFT), instead of using the wave function as the primary variable, the electron density ($\rho(\vec{r})$) which itself is a function of coordinate, is used as a *functional* in the calculation of the ground state energy. As mentioned at the beginning of this chapter, DFT is the result of two main theorems which were developed by P. Hohenberg and W. Kohn and then became practical with the formalisms introduced by W. Kohn and L. J. Sham. However, the starting point and idea of DFT originates from the Thomas-Fermi model. Hence, before further discussions on the details of DFT, the Thomas-Fermi model is explained.

Thomas-Fermi Model

The electron density in a volume element ($d\vec{r}_1$) for a **n**-electron system over the spin coordinates is defined as:

$$\rho(\vec{r}_1) = n \int \cdots \int |\Psi\{(\vec{r}_1), (\vec{r}_2), ..., (\vec{r}_{\mathrm{n}})\}|^2 ds_1 d\vec{r}_2 ... d\vec{r}_{\mathrm{n}}. \tag{2.1.16}$$

This definition is the core of density based methods which is reflected in the calculation of ground state energy. Based on the Eq. 2.1.16, the total number of electrons in the system (n) over the entire space can be obtained by:

$$n = \int \rho(\vec{r}) d\vec{r}. \tag{2.1.17}$$

In the first steps towards DFT, Thomas and Fermi [66, 67] used this concept to develop their model for the calculation of the ground state energy as a functional of electron density. They assumed that the kinetic energy of electrons can be estimated using the

kinetic energy of the homogeneous electron gas. The formulation for the kinetic energy was then proposed as:

$$T_{\mathrm{TF}}[\rho(\vec{r})] = \frac{3}{10}(3\pi^2)^{\frac{2}{3}} \int \rho^{\frac{5}{3}}(\vec{r})d\vec{r}. \tag{2.1.18}$$

By combining Eq. 2.1.18 with the attractive nuclei-electron and repulsive electron-electron interactions, the total ground state energy of a system as a functional of its electron density can be obtained as:

$$E_{\mathrm{TF}}[\rho(\vec{r})] = \frac{3(3\pi^2)^{\frac{2}{3}}}{10} \int \rho^{\frac{5}{3}}(\vec{r})d\vec{r} - Z\int \frac{\rho(\vec{r})}{r}d\vec{r} + \frac{1}{2}\int\int \frac{\rho(\vec{r_1})\rho(\vec{r_2})}{r_{12}}d\vec{r_1}d\vec{r_2}. \tag{2.1.19}$$

Despite the fact that Eq. 2.1.19 is the building block of modern DFT, it suffers from significant crude approximations, such as the description of kinetic energy and also disregarding the exchange and correlation effects. The exchange interaction effects for the homogeneous electron gas were introduced into the Eq. 2.1.19 later by Dirac as:

$$E_{\mathrm{x}}^{\mathrm{D}} = -\frac{3}{4}\left(\frac{3}{\pi}\right)^{\frac{1}{3}} \int \rho(\vec{r})^{\frac{4}{3}}d\vec{r}. \tag{2.1.20}$$

As the result of this contribution (the model is then referred to as Thomas-Fermi-Dirac), the total energy decreases due to the negative sign of Dirac exchange term. Nevertheless, because of massive approximations, this model fails to yield the correct calculations of the total energy in most systems.

2.1.5 The Hohenberg–Kohn Theorems

Hohenberg and Kohn [52] developed the idea of Thomas-Fermi model in a more detailed and accurate approach. In their first theorem, Hohenberg and Kohn proved that the electron density of a system can uniquely determine the Hamiltonian and consequently the ground state energy and other properties of that system. In other words, they stated that "the external potentials of electrons and nuclei is a unique functional of $\rho_0(\vec{r})$" [52]. Therefore, the following relation can be concluded:

$$\rho_0(\vec{r}) \rightarrow \hat{H} \rightarrow E_0. \tag{2.1.21}$$

Based on this theorem, the total energy as a functional of electron density can be written as:

$$\begin{aligned} E_0[\rho_0(\vec{r})] &= T[\rho_0(\vec{r})] + E_{\mathrm{e-nu}}[\rho_0(\vec{r})] + E_{\mathrm{e-e}}[\rho_0(\vec{r})], \\ E_0[\rho_0(\vec{r})] &= \underbrace{\int \rho_0(\vec{r})V_{\mathrm{ext}}(\vec{r})d\vec{r}}_{\text{particular system}} + \underbrace{T[\rho_0(\vec{r})] + E_{\mathrm{e-e}}[\rho_0(\vec{r})]}_{\text{every system}=F_{\mathrm{HK}}[\rho_0(\vec{r})]}. \end{aligned} \tag{2.1.22}$$

$F_{\mathrm{HK}}[\rho_0(\vec{r})]$ (Hohenberg-Kohn functional), which is a system independent energy term, includes the contributions of kinetic and electron-electron repulsion energies. If we were able to exactly solve this problem, we could obtain the exact answer to the Schrödinger equation. The repulsive electron-electron term can be written as:

$$E_{\mathrm{e-e}}[\rho_0(\vec{r})] = \underbrace{\frac{1}{2}\int\int \frac{\rho_0(\vec{r}_1)\rho_0(\vec{r}_2)}{\vec{r}_{12}} d\vec{r}_1 d\vec{r}_2}_{J[\rho_0(\vec{r})]} + E_{\mathrm{qm}}[\rho_0(\vec{r})], \tag{2.1.23}$$

in which the term $E_{\mathrm{qm}}[\rho_0(\vec{r})]$ refers to all the quantum mechanical contributions including the electron-electron correlations, exchange and self interactions, while $J[\rho_0(\vec{r})]$ is the classical Coulomb interaction.

The second theorem of Hohenberg and Kohn is basically another description of variational principle. It states that Eq. 2.1.22 for any electron density of $\rho(\vec{r})$ results in an upper bound to the ground state energy ($E[\rho(\vec{r})] \geq E_0[\rho_0(\vec{r})]$). Clearly, the preliminary conditions for electron density to be a valid value (i.e. $\rho(\vec{r}) \geq 0$ and $\int \rho(\vec{r}) d\vec{r} = n$) are still required. It can be seen that DFT is a ground state theory which cannot deal with excited states. Despite the fact that so far the formulation is reasonable, it is still not possible to obtain the universal description for Hohenberg and Kohn functional, i.e. $F_{\mathrm{HK}}[\rho_0(\vec{r})]$. In the following section, it is shown how the formalism of Kohn-Sham leads to a practical method for dealing with quantum mechanical concepts of electron-electron exchange and correlation functionals.

2.1.6 The Kohn-Sham Approach

Kohn and Sham [53] proposed a method to deal with Eq. 2.1.22 derived from the Hohenberg and Kohn theorems. In fact, they focused on how to consider the kinetic energy part since it can introduce large deviations in the total energy. The most distinguished assumption by Kohn and Sham was the fact that since it is not possible to obtain the exact true kinetic energy of an interacting system ($T[\rho_0(\vec{r})]$), this term can be divided into two parts: One part is the kinetic energy of a non-interacting system (T_{S}) and the other is the remaining effects corresponding to the interacting system ($T - T_{\mathrm{S}}$). Therefore, the proposed kinetic energy part by Kohn-Sham can be written as

$$T_{\mathrm{S}} = -\frac{1}{2}\sum_{i=1}^{\mathrm{n}} \langle \phi_i^{\mathrm{KS}} | \nabla^2 | \phi_i^{\mathrm{KS}} \rangle, \tag{2.1.24}$$

in which n is the number of electrons in the system and ϕ_i^{KS} represents one-electron Kohn-Sham spin orbitals. Therefore, the Hohenberg-Kohn functional, $F_{\mathrm{HK}}[\rho(\vec{r})]$, can be

written as:

$$F_{\mathrm{HK}}[\rho(\vec{r})] = T_{\mathrm{S}}[\rho(\vec{r})] + J[\rho(\vec{r})] + E_{\mathrm{XC}}[\rho(\vec{r})]. \tag{2.1.25}$$

In this important formalism, $E_{\mathrm{XC}}[\rho(\vec{r})]$ is the sum of $(T - T_S)$, electron-electron self-interaction, exchange and correlation effects, all of which are unknown quantities. Therefore, the total energy can be written as:

$$E[\rho(\vec{r})] = T_{\mathrm{S}}[\rho(\vec{r})] + J[\rho(\vec{r})] + E_{\mathrm{XC}}[\rho(\vec{r})] + \underbrace{\int \rho(\vec{r}) V_{\mathrm{ext}}(\vec{r}) d\vec{r}}_{E_{\mathrm{e-nu}}[\rho(\vec{r})]}. \tag{2.1.26}$$

Now the V_{eff} should be defined in such a way that the resulting one-electron Kohn-Sham spin orbitals exactly provide the density of the real system. For this, we refer to Eqs. 2.1.24 and 2.1.26 and expand Eq. 2.1.26 as:

$$\begin{aligned} E[\rho(\vec{r})] = & \underbrace{-\frac{1}{2}\sum_{i=1}^{n} \langle \phi_i^{\mathrm{KS}} | \nabla^2 | \phi_i^{\mathrm{KS}} \rangle}_{T_{\mathrm{S}}[\rho(\vec{r})]} + \underbrace{\frac{1}{2}\sum_{i=1}^{n}\sum_{j=1}^{n} |\phi_i^{\mathrm{KS}}(\vec{r}_1)|^2 \frac{1}{r_{12}} |\phi_j^{\mathrm{KS}}(\vec{r}_2)|^2 d\vec{r}_1 d\vec{r}_2}_{J[\rho(\vec{r})]} \\ & + E_{\mathrm{XC}}[\rho(\vec{r})] \underbrace{- \sum_{i=1}^{n} \int \sum_{A=1}^{m} \frac{Z_A}{r_{1A}} |\phi_i^{\mathrm{KS}}(\vec{r}_1)|^2 d\vec{r}_1}_{E_{\mathrm{e-nu}}[\rho(\vec{r})]}. \end{aligned} \tag{2.1.27}$$

Finally, the variational principle is applied to the total Hamiltonian and minimum energy eigenvalues (ϵ_i) can be obtained as:

$$\Bigg[-\frac{1}{2}\nabla^2 + \overbrace{\Bigg(\int \frac{\rho(\vec{r_2})}{r_{12}} d\vec{r}_2 - \underbrace{\sum_{A=1}^{M} \frac{Z_{\mathrm{A}}}{r_{1\mathrm{A}}}}_{V_{\mathrm{ext}}} + V_{\mathrm{XC}}(\vec{r}_1) \Bigg)}^{V_{\mathrm{eff}}} \Bigg] \phi_i^{\mathrm{KS}} = \epsilon_i \phi_i^{\mathrm{KS}}, \tag{2.1.28}$$

where the electron density of the real system can be expressed from the Kohn-Sham spin orbitals as:

$$\rho(\vec{r}) = \sum_{i=1}^{\mathrm{n}} |\phi_i^{\mathrm{KS}}(\vec{r})|^2, \tag{2.1.29}$$

with n equals to the number of electrons. Eqs. 2.1.28 and 2.1.29 are referred to as the **Kohn-Sham equations**. In Eq. 2.1.28, V_{eff} is the effective potential in which only $V_{\mathrm{XC}}(\vec{r})$ (potential due to the exchange-correlation energy equal to $\frac{\delta E_{\mathrm{XC}}[\rho(\vec{r})]}{\rho(\vec{r})}$) term is unknown. Unlike the Hartree-Fock scheme where the approximations are entered from the first step because of the nature of the Slater determinant, in the Kohn-Sham formulations it is only after Eq. 2.1.28 where the approximations are introduced. If finding the exact value for E_{XC} were possible, the ground state energy obtained from DFT would be close to the exact value. Finding the exact value for E_{XC} has not been successful so far while development

in this area is an ongoing field of research. To sum up, the overall procedure to solve the Kohn-Sham equations for a fixed geometry (single-point calculation) is as the following sequence:

- Starting with an initial $\rho(\vec{r})$,
- Obtaining the V_{eff} and determining a new $\rho(\vec{r})$ using Eqs. 2.1.28 and 2.1.29,
- Using the obtained Kohn-Sham orbitals from Eq. 2.1.28 to calculate the kinetic energy via Eq. 2.1.24,
- Continuing this cycle until $\rho(\vec{r})$ is converged within a certain criterion and then total energy can be calculated using Eq. 2.1.27.

In the next section, various approaches for finding the exchange correlation energy functional are discussed and it is shown how each of them can be beneficial for a specific system (metallic, insulator, semiconductor etc).

2.1.7 Exchange-Correlation Energy Functionals

A simple approach to deal with the XC energy functional is the **local density approximation (LDA)**. In the LDA, based on the homogeneous electron gas model, it is assumed that in the XC energy of an inhomogeneous system, the electron density can be treated **locally** as the electron density of a homogeneous electron gas [68]. The homogeneous electron gas model is defined as a hypothetical system where the electrons move in the field of a uniform positive background charge (atomic nuclei) which prevails the charge neutrality condition while the electron density is uniform. Hence, the XC energy using the LDA description can be written as:

$$E_{\text{XC}}^{\text{LDA}}[\rho(\vec{r})] = \int \rho(\vec{r})\epsilon_{\text{XC}}[\rho(\vec{r})]d^3\vec{r}, \tag{2.1.30}$$

in which, $\epsilon_{\text{XC}}[\rho(\vec{r})]$ is the exchange-correlation energy per particle of a uniform electron gas. This expression can be divided into two parts, namely exchange and correlation as:

$$\epsilon_{\text{XC}}[\rho(\vec{r})] = \epsilon_{\text{X}}[\rho(\vec{r})] + \epsilon_{\text{C}}[\rho(\vec{r})]. \tag{2.1.31}$$

The exchange part which is in fact derived from the HF scheme was given by Dirac [69] as:

$$\epsilon_{\text{X}}[\rho(\vec{r})] = -\frac{3}{4}\left(\frac{3}{\pi}\right)^{\frac{1}{3}} \int \rho^{\frac{3}{4}}(\vec{r})d^3\vec{r}. \tag{2.1.32}$$

The correlation part was calculated for the homogeneous electron gas by Ceperly and Alder using numerical calculations in quantum Monte Carlo simulations [70]. An accurate description of Coulomb correlation within the LDA was given by Perdew and Wang [71]. It is known that the LDA delivers rather reasonable results in case of prediction of equilibrium structures or frequencies. When it comes to binding and cohesive energies, however, it usually fails. Especially in case of structures with highly non-uniform electron densities, the LDA is rather a poor approximation [72, 73].

In order to deal with more complex and non-homogeneous electron densities, **generalized gradient approximation (GGA)** was introduced [74, 75]. This approach, which is an improvement over the LDA, is widely used in surface science and solid states physics due to its accuracy and efficiency. The key aspect in the GGA is the addition of density gradient to the LDA description. Therefore, it can be written as the following expression:

$$E_{\mathrm{XC}}^{\mathrm{GGA}}[\rho(\vec{r})] = \int f\left[\rho(\vec{r}), \nabla\rho(\vec{r})\right] d^3\vec{r} = E_{\mathrm{X}}^{\mathrm{GGA}}[\rho(\vec{r})] + E_{\mathrm{C}}^{\mathrm{GGA}}[\rho(\vec{r})]. \tag{2.1.33}$$

One of the popular forms of the GGA functional is the one proposed by Perdew, Burke, and Ernzerhof (PBE) [75], which is widely used in theoretical material science. The exchange term of the PBE functional is written as:

$$E_{\mathrm{X}}^{\mathrm{GGA}}[\rho(\vec{r})] = \int \rho(\vec{r}) F_{\mathrm{X}}(s_\sigma) \epsilon_{\mathrm{X}}^{\mathrm{unif}}[\rho(\vec{r})] d^3\vec{r}, \tag{2.1.34}$$

in which, $\epsilon_{\mathrm{X}}^{\mathrm{unif}}[\rho(\vec{r})]$ is the exchange energy of the homogeneous gas per particle which is defined as:

$$\epsilon_{\mathrm{X}}^{\mathrm{unif}}[\rho(\vec{r})] = \frac{-3e^2 k_F}{4\pi} \quad , \quad \rho(\vec{r}) = \frac{3}{4}\pi r_s^3 = \frac{k_F^3}{3\pi^2} \quad , \quad r_s = \text{local Seitz radius.} \tag{2.1.35}$$

In Eq. 2.1.34, the $F_X(s_\sigma)$ function is described as:

$$F_X(s_\sigma) = 1 + \kappa - \frac{\kappa}{1 + \frac{\mu s^2}{\kappa}} \ , \ \kappa \approx 0.804 \ , \ \mu \approx 0.219, \tag{2.1.36}$$

in which s is a dimensionless density gradient as:

$$s = \frac{|\nabla\rho(\vec{r})|}{2 \times (3\pi^2\rho(\vec{r}))^{\frac{1}{3}} \times \rho(\vec{r})}. \tag{2.1.37}$$

The correlation part of the energy is also obtained using the following equation:

$$E_{\mathrm{C}}^{\mathrm{GGA}}[\rho(\vec{r})] = \int \rho(\vec{r}) \left[\epsilon_{\mathrm{C}}^{\mathrm{unif}}[\rho(\vec{r})] + H[\rho(\vec{r}), w]\right] d^3\vec{r}. \tag{2.1.38}$$

In this equation, $H[\rho(\vec{r}), w]$ is defined by:

$$H[\rho(\vec{r}), w] = \gamma \times \ln\left(1 + \frac{\beta w^2}{\gamma}\left[\frac{1 + Aw^2}{1 + Aw^2 + A^2 w^4}\right]\right), \tag{2.1.39}$$

where,

$$\gamma \approx 0.031,\ \ \beta \approx 0.066,\ \ w = \frac{|\nabla\rho(\vec{r})|}{2\rho(\vec{r})\sqrt{\frac{4(3\pi^2\rho(\vec{r}))^{\frac{1}{3}}}{\pi}}},\ \ A = \frac{\beta}{\gamma[\exp(\frac{-\epsilon_C^{\text{unif}}}{\gamma}) - 1]}. \tag{2.1.40}$$

The sum of $E_{\text{C}}^{\text{GGA}}[\rho(\vec{r})]$ and $E_{\text{X}}^{\text{GGA}}[\rho(\vec{r})]$ yields the PBE-GGA exchange correlation functional.

Although the GGA is one of the most successful exchange-correlation energy functionals for DFT, it still has few drawbacks. One of the most dramatic ones is referred to the highly delocalized nature of this approximation. A famous example in which DFT and conventional band theory fail to predict is the **Mott insulators** [76]. According to the conventional band theory and DFT predictions, Mott insulators are "expected" to be electrically conductive, however, they practically behave as insulators. This can be explained by considering the fact that in these highly correlated systems, where electron-electron correlations are highly dominant, due to the over-delocalizing of the valence electrons and over-stabilizing of the metallic ground states with the LDA or GGA, Mott insulators are incorrectly predicted to be conductive [77]. This is also related to the fact that in the LDA and GGA, electron self interaction is not canceled out hence a massive delocalization is introduced in the Kohn-Sham orbitals. Besides computationally demanding methods such as DFT plus dynamical mean field theory (DFT+DMFT) [78] or reduced density matrix functional theory (RDMFT) [79] which can solve problems raised in cases such as Mott insulators, a simple yet effective method based on the **Hubbard** model, namely the **LDA+U** was developed which is very popular in case of the systems with highly correlated electronic structures [80]. The Hubbard model which is based on the **tight-binding** approach, introduces two main assumptions, namely the kinetic or hopping integral (shown by *t*) and on-site repulsive Coulomb interaction of electrons. The Hubbard Hamiltonian is formulated as [81]:

$$\hat{H}_{\text{Hub}} = -t \sum_{\langle i,j\rangle,m_s} (c_{i,m_s}^{\dagger} c_{j,m_s} + c_{j,m_s}^{\dagger} c_{i,m_s}) + U \sum_{i=i}^{N} n_{i\uparrow} n_{i\downarrow} - \mu \sum_{i} (n_{i\uparrow} + n_{i\downarrow}). \tag{2.1.41}$$

In this Hamiltonian, $\langle i, j\rangle$ refers to the nearest-neighbor sites which implies that the hopping is only allowed between two adjacent sites. $c_{i,m_s}^{\dagger}$, c_{j,m_s} and n_{i,m_s} represent the electronic creation, annihilation and number operators of electrons with spin m_s on site i. In fact the first term represents the kinetic energy, the second term refers to the interaction energy (if one site is doubly occupied, it adds an energy value of U) and the last term controls the filling of orbitals and corresponds to the chemical potentials (μ).

The LDA+U (which is the same for GGA+U), based on the Hubbard model can then be formulated as:

$$E_{\mathrm{LDA+U}}(\rho) = E_{\mathrm{LDA}}(\rho) + E_{\mathrm{Hub}}\left[n^{Im_s}_{mm'}\right] - E_{DC}\left[n^{Im_s}\right], \tag{2.1.42}$$

in which, E_{Hub} is the energy term derived from the Hubbard Hamiltonian and E_{DC} is the energy term that cancels out the terms that are already contained in the E_{LDA} in order to avoid double counting. After few mathematical steps, the final form of the LDA+U exchange correlation functional energy based on the refined model presented by Dudarev [82] (which is the one used in this thesis) is written as:

$$E_{\mathrm{LDA+U}}(\rho) = E_{\mathrm{LDA}}(\rho) + \frac{(\bar{U}-\bar{J})}{2}\sum_{m_s}\left[\left(\sum_{j}\rho^{m_s}_{jj}\right) - \left(\sum_{j,l}\rho^{m_s}_{jl}\rho^{m_s}_{lj}\right)\right], \tag{2.1.43}$$

where $\rho^{m_s}_{jl}$ is the density of *d*-orbital electrons. $\bar{U}$ and $\bar{J}$ are the averaged matrix elements of the Coulombic electron-electron interaction (in eV). In the Dudarev formulation, $\bar{U}$ and $\bar{J}$ values alone are not meaningful and $(\bar{U}-\bar{J})$ should be considered.

In this thesis, the LDA (mostly for comparison and benchmark), the PBE and the PBE+U exchange correlation energy functionals are used. The first two are implemented in `SeqQuest` [83] while all three are available in `VASP` [84].

2.1.8 Schrödinger Equation for Periodic Systems

Up to now, the methods and approximation techniques for solving the Schrödinger equation in a system of atoms are presented. In the following section, it is demonstrated how to apply same approaches for the extended solids (crystals). The key concept to deal with these periodic systems is the **Bloch theorem**. Before going into the details of Bloch theorem, a few remarks in the context of periodic systems should be explained.

In this thesis, for 3D modeling of bulk solids periodic supercells are applied. This approach implies that a supercell is wrapped around itself in such a way that when one particle goes out from one side, it immediately comes back from the other side. One drawback of the supercell approach is the *finite unit cell size effect* which is extensively dealt with in this thesis. For 2D modeling of surfaces the **slab** technique (Fig. 4) is employed. A slab has the immediate periodicity in *x* and *y* directions but in the *z* direction a vacuum level (normally with about 14 Å thickness) is defined in order to mimic the surface condition while keeping the structure in a 3D periodic format at the same time.

Therefore, it is possible to apply the Bloch theorem in a slab as well. For modeling an isolated atom (0D) a large box including the desired atom is considered and only a single-point calculation is performed. In this thesis, 1D modeling of a system is not performed.

Ideal crystals are formed by a 3D ordering of atoms and are constructed from unit cells (smallest repeating unit in a crystal). In crystals, depending on the degree of crystallinity, there can be long- or short-range order between unit cells. An ideal crystal is composed of a basis and a lattice. Basis is referred to each of the identical group of atoms that form an ideal crystal. A lattice is a group of points which are extended in space based on a mathematical description. The basis vectors, $\vec{a_1}$, $\vec{a_2}$ and $\vec{a_3}$, form lattice vectors, T, as [85]:

$$\vec{T} = u_1\vec{a_1} + u_2\vec{a_2} + u_3\vec{a_3} \quad \text{with} \quad u_1, u_2, u_3 \quad \text{as integers.} \tag{2.1.44}$$

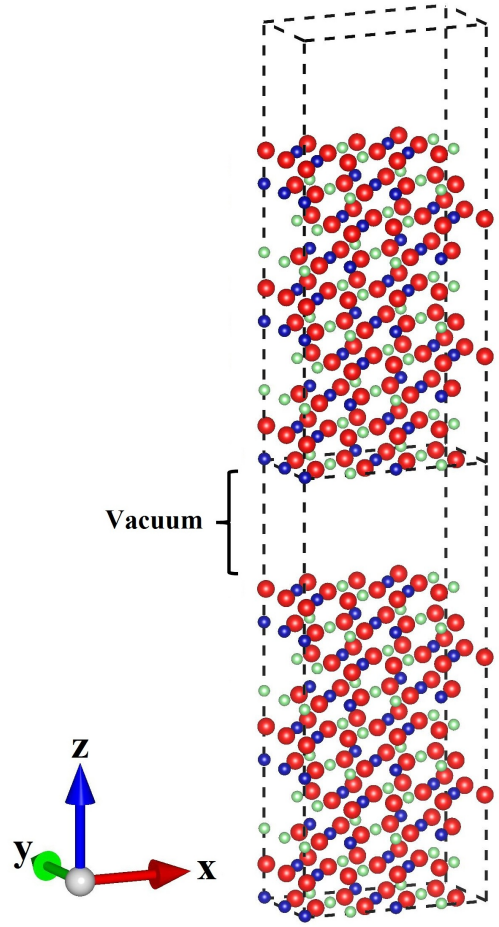

Figure 4: 3D view of a slab model in case of $LiCoO_2(10\bar{1}4)$ surface. Li, O and Co ions are shown with light green, red and blue colors, respectively.

In a crystal and according to the Bloch theorem, the Kohn-Sham effective potential (V_{eff}, see Eq. 2.1.28) can be written as a periodic potential acting on the electrons:

$$V_{\text{eff}}(\vec{r} + \vec{T}) = V_{\text{eff}}(\vec{r}). \tag{2.1.45}$$

This periodic potential can then be introduced in the Hamiltonian of the Kohn-Sham formalism (Eq. 2.1.28) as:

$$\hat{H}\phi_i^{\text{KS}} = \Big(-\frac{1}{2}\nabla^2 + \underbrace{V_{\text{eff}}(\vec{r} + \vec{T})}_{V_{\text{eff}}(\vec{r})} \Big)\phi_i^{\text{KS}} = \epsilon_i \phi_i^{\text{KS}}. \tag{2.1.46}$$

2.1.9 Bloch Theorem

As it was demonstrated in the previous part, the Kohn-Sham effective potential can be written as a periodic function and for crystals can be directly introduced in the Kohn-Sham equations. Now it is shown how this concept can be transfered to the wave functions.

Within the Bloch theorem [86] it can be proved that the electronic eigenstates of Eq. 2.1.46 (Kohn-Sham orbitals, ϕ^{KS}, also shown in Eq. 2.1.29) can be written in the form of a plane wave multiplied by a function with the periodicity of the Bravais lattice. Therefore, ϕ^{KS} can be written as:

$$\phi^{\mathrm{KS}}_{n,\vec{k}}(\vec{r}) = e^{i\vec{k}\cdot\vec{r}} v_{n,\vec{k}}(\vec{r}), \tag{2.1.47}$$

in which, n is the band index, $\vec{k}$ is the wave vector within the first Brillouin zone and $v_{n,\vec{k}}(\vec{r}+\vec{T}) = v_{n,\vec{k}}(\vec{r})$. Another formulation of the Bloch theorem can be presented as:

$$\phi^{\mathrm{KS}}_{n,\vec{k}}(\vec{r}+\vec{T}) = e^{i\vec{k}.\vec{T}} \phi^{\mathrm{KS}}(\vec{r}). \tag{2.1.48}$$

The periodic potential $v_{n,\vec{k}}(\vec{r})$ can also be written as a set of plane waves:

$$v_{n,\vec{k}}(\vec{r}) = \sum_{G} c_{n,\vec{k}}\, e^{i\vec{k}.\vec{r}} \cdot \vec{G} \quad \text{with} \quad \vec{G}\cdot\vec{T} = 2\pi m, \tag{2.1.49}$$

where $\vec{G}$ and $\vec{T}$ are the reciprocal and real space lattice vectors, respectively. m is an integer and $c_{n,\vec{k}}$ are the plane wave expansion coefficients. Finally, the electronic eigenstates of Eq. 2.1.46 can be written as a linear combination of plane waves as:

$$\phi^{\mathrm{KS}}_{n,\vec{k}}(\vec{r}) = \sum_{G} c_{n,\vec{k}}\, \vec{G} \cdot e^{i(\vec{k}+\vec{G}).\vec{r}}. \tag{2.1.50}$$

It should be noted that by expanding the electronic wave function in the form of plane waves basis set, Kohn-Sham equations become simpler and more adoptable to Bloch theorem [85].

2.1.10 Sampling of the Brillouin Zone

To obtain the properties of a solid (e.g. charge density or density of states), integration of the Brillouin zone in reciprocal space is necessary. However, since it is computationally impossible to integrate over all the points in space, numerical integration (weighted sum) using the sampling of the Brillouin zone is a practical approach to deal with this problem. Therefore, the electron density can be expressed as the following expression:

$$\rho(\vec{r}) = \sum_{i=1}^{\text{occupied}} \int_{\mathrm{BZ}} |\phi^{\mathrm{KS}}_{n,\vec{k}}(\vec{r})|^2 \frac{d^3\vec{k}}{\Omega_{\mathrm{BZ}}} \approx \sum_{i=1}^{\text{occupied}} \sum_{j=1}^{N_{\mathrm{kpt}}} \omega_n |\phi^{\mathrm{KS}}_{n,\vec{k}}(\vec{r})|^2. \tag{2.1.51}$$

In this equation and in the framework of DFT, $\phi^{\mathrm{KS}}_{n,\vec{k}}(\vec{r})$ are the Kohn-Sham orbitals, Ω_{BZ} is the cell volume and ω_n are the weighting factors (or "importance" factors adopted from the weighted sum model). To reduce error, dense k-points sampling is preferred at the expense of computational cost. Therefore, convergence tests are always necessary to

create a balance between the accuracy of data and the computing time. One of the popular methods for sampling the Brillouin zone is the approach proposed by Monkhorst and Pack [87] in which homogeneous k-points in the Brillouin zone and along the three axes of reciprocal space are considered.

2.1.11 Pseudopotential Method

In order to minimize the computational efforts, instead of considering all of the electrons in atoms, only the valence ones are explicitly treated and the rest (inner electrons and nuclei) are replaced by an effective potential. This effective potential is referred to as **pseudopotential**. In general, Kohn-Sham orbitals near the nuclei regions show significantly large and sharp oscillations which are caused by the requirement of orthogonality. In order to describe this behavior correctly, using large plane wave sets (or a fine real-space mesh grid for the numerical integration) is necessary. However, since using large plane wave sets is computationally expensive, it can be replaced by a smooth effective potential near the core regions. In fact, while the core electrons are "*frozen*", the chemically-active valence electrons are treated by pseudo-wave functions with fewer nodes [88]. As a result, the pseudo-wave functions can be expressed with fewer Fourier transforms (see Eq. 2.1.49). There are several methods for the development of pseudopotentials, such as norm-conserving, ultrasoft, projector-augmented wave method which in the following sections are briefly discussed. In this thesis, the norm-conserving and projector-augmented wave (PAW) methods are employed which are implemented in `SeqQuest` and `VASP`, respectively.

Norm-Conserving Pseudopotentials

One type of pseudopotentials is the norm-conserving which is used in both atomic orbitals and plane-wave DFT codes [89]. Norm-conserving pseudopotentials must have the following criteria:

- Pseudo and real eigenvalues of the valence electrons for an specific atom match each other.
- Norm of each pseudo-wave function beyond a chosen cut-off radius (r_c) (valence electrons) matches its corresponding real wave function.
- The integrals of the pseudo and real charge densities from 0 to r ($r > r_c$) of each valence state (norm conservation) should be in agreement.

Nevertheless, in this type of pseudopotentials due to large oscillations of wave function around the core regions, many plane waves are still needed to fulfill the above requirements which makes it computationally demanding [89].

Projector Augmented Wave Method

An accurate and efficient method for creating pseudopotentials is based on the method developed by Blöchl [90] which is referred to as **Projector augmented-wave (PAW)**. In this method, by defining a linear transformation operator ($\hat{T}$), the true all-electron Kohn-Sham wave function ($\phi^{\mathrm{KS}}_{n,\vec{k}}(\vec{r})$) can be converted to an auxiliary smooth wave function ($\tilde{\phi}^{\mathrm{KS}}_{n,\vec{k}}(\vec{r})$) by:

$$|\tilde{\phi}^{\mathrm{KS}}_{n,\vec{k}}(\vec{r})\rangle = \hat{T}|\phi^{\mathrm{KS}}_{n,\vec{k}}(\vec{r})\rangle. \tag{2.1.52}$$

In fact using this approach, the original Kohn-Sham wave function is split into a fully-expanded smoothed auxiliary wave function and a confined rapid-oscillating contribution (only in certain areas in space). The former can be treated with coarse grids which significantly accelerates the calculations.

2.1.12 Basis Sets

In the present thesis, DFT calculations are performed using `VASP` and `SeqQuest` codes with two different basis sets, namely plane wave and localized atomic orbital, respectively. In the following a brief overview of these basis sets is presented.

In Eq. 2.1.28, beside using numerical methods, another approach to make the calculations computationally feasible is to expand the Kohn-Sham orbitals via a linear combination of analytic functions, χ^{LCAO}, called **linear combination of atomic orbitals (LCAO)** [91]:

$$\phi^{\mathrm{KS}}_i = \sum_{j=1}^{N_{\mathrm{basis}}} c_{ij}\chi^{\mathrm{LCAO}}_j, \tag{2.1.53}$$

where N_{basis} and c_{ij} are the number and coefficients of basis functions, respectively. In principle, if an infinite number of basis functions could be used, the exact Kohn-Sham orbitals would be obtained. Nevertheless, usually a certain number of basis functions is employed which balances between both accuracy and computational speed. Using the LCAO method, the Kohn-Sham equations can be converted from a non-linear to a linear eigenvalue problem as [91]:

$$\hat{F}_{\mathrm{KS}}C = \hat{S}C\epsilon_i, \tag{2.1.54}$$

where C is the expansion coefficient matrix, ϵ_i is the diagonal matrix of Kohn-Sham orbital energies and the two operators of $\hat{F}^{\mathrm{KS}}$ (Kohn-Sham matrix) and $\hat{S}$ (overlap matrix) are defined as below [91]:

$$\begin{aligned} \hat{F}_{ij}^{\mathrm{KS}} &= \int \chi_i^{*\mathrm{LCAO}}(\vec{r}) \Big[-\frac{1}{2}\nabla^2 + V_{\mathrm{eff}}(\vec{r}) \Big] \chi_j^{\mathrm{LCAO}}(\vec{r}) d\vec{r}, \\ \hat{S}_{ij} &= \int \chi_i^{*\mathrm{LCAO}}(\vec{r}) \chi_j^{\mathrm{LCAO}}(\vec{r}) d\vec{r}. \end{aligned} \tag{2.1.55}$$

Usually, in most of the density- and wave function-based methods, the basis functions have the general form of **Gaussian-type-orbitals (GTO)** which in the cartesian coordinate (x, y, z) are given by [91]:

$$\chi_{\mathrm{GTO}}(\vec{r}) = N x^l y^m z^n e^{-\alpha r^2}, \tag{2.1.56}$$

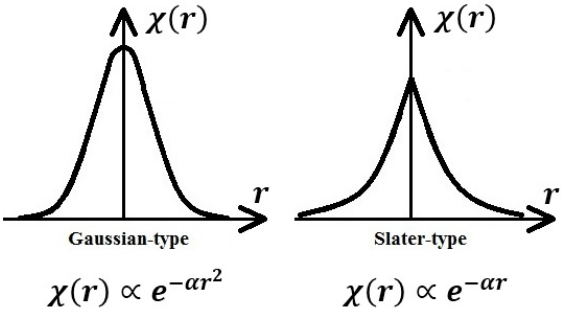

Figure 5: Plots of STO and GTO basis functions.

where N is a normalization factor, α is the orbital exponent and $L = l + m + n$ is the angular quantum number. Since there are many efficient algorithms to solve eigenvalue problems using the GTO basis functions, these basis sets are popular. Another popular set of basis functions are referred to as **Slater-type-orbitals (STO)** since they reflect an exact representation of the hydrogen atomic orbital. Moreover, their functions show a correct cusp behavior as a discontinuous derivative at $r = 0$ with an exponential decay while the GTO has a zero slope at $r = 0$ point with a rather steeper decay (see Fig. 5). The STO basis functions in spherical coordinates (r, θ, ϕ) have the following form:

$$\chi_{\mathrm{STO}} = N Y_{lm}(\theta, \phi) r^{n-1} e^{-\alpha r}, \tag{2.1.57}$$

where $Y_{lm}(\theta, \phi)$ represents the spherical harmonics for the angular momentum part and the rest are similar to the GTO. It has been shown that in order to achieve reliable results, the number of basis functions in the form of the GTO must be 3 times larger than the STO [92]. Due to lack of analytical integrals for the STOs, however, they have to be dealt with numerically. In order to have the advantages of both of these basis functions, **contracted Gaussian functions (CGF)** consisted of several Gaussian functions were introduced. The contraction coefficient can be chosen in a way that the whole basis sets mimic the features of STOs. The `SeqQuest` DFT code which is used in several parts of this thesis, employs CGF basis functions. In particular, its basis orbitals are real spherical harmonics multiplied by CGF basis functions.

It is also well established to employ non-localized **plane wave** basis sets which are expanded through the whole space. The general and extended form of plane wave are provided in section 2.1.9, Eqs. 2.1.47 and 2.1.50. In principle, an infinite number of plane waves is required for the expansion of Bloch wave function. However, in real applications, it is limited to a certain number of plane waves which can be determined in such a way that includes only those with kinetic energies smaller than a desired specific energy cutoff (in eV) according to:

$$E_{\text{cutoff}} \geq \frac{\hbar^2}{2m}|\vec{G}|^2. \tag{2.1.58}$$

Many of the calculations in the present thesis were performed using `VASP` DFT code which employs plane wave basis sets.

2.2 Ionic Conductivity

As mentioned earlier, ionic and electronic conductivity play an important role in determining the performance of battery systems. In this section, an overview of the mechanisms of formation and migration of defects is presented and it is discussed how using *ab initio*-based calculations, these properties can be evaluated. In fact via **multiscale modeling**, macroscopic properties such as conductivity can be estimated using the inputs which are obtained from *ab initio*-based calculations.

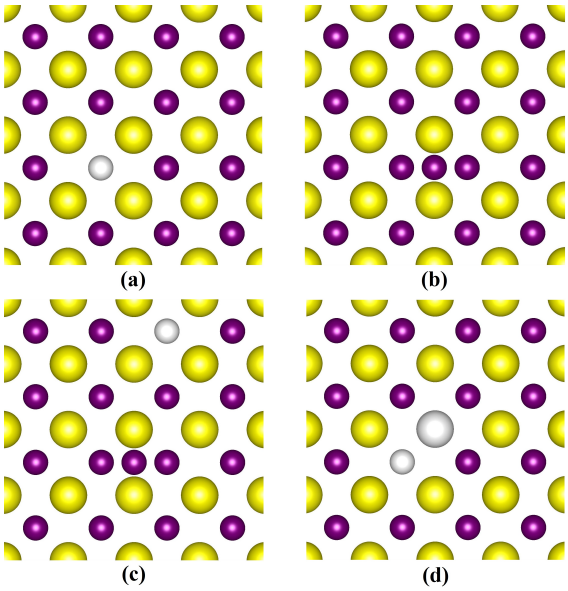

Figure 6: Four most common defect types in solids in the case of Li_2S. (a) Li vacancy (b) interstitial Li (c) Li Frenkel pair and (d) Schottky defects. Li, S and Li-vacancy are shown with violet, yellow and white, respectively.

In a defective crystal, ions (or defects) migration can mainly take place via the **vacancy** or the **interstitial** hopping mechanisms [4]. In the vacancy mechanism, due to thermal driven vibrations, an ion from a defect-free crystal is removed and a vacant site is created. Another nearby ion can then hop to this vacant site and fill it, while leaving its original position empty. This is also considered as vacancy diffusion, although the actual movement belongs to the ion. In the interstitial mechanism, thermal vibrations of ions may cause another ion to move out from its equilibrium position, occupies an interstitial site and

finally hops to the next nearest interstitial site. If the original site becomes empty (formation of vacancy), the combination of these two defects (vacancy and interstitial) forms a **Frenkel** pair defect and is usually referred to as the Frenkel mechanism. This type usually forms in solids in which anions are much larger than cations (e.g. ZnS). In the **Schottky** mechanism, which is in fact formation of vacancies, a pair of cation and anion is missing from the lattice. This type often appears in solids in which the sizes of anions and cations are similar (e.g. KCl) (see Fig. 6). An especial form of an interstitial mechanism, which occurs in a cooperative multi-particle manner with a synchronized fashion and is usually observed in solid electrolytes, is referred to as the **"knock-off"** mechanism [93]. Depending on the type and nature of a crystal, any of the mentioned mechanisms might have lower activation energy, i.e. sum of the formation and migration energies, and thus could be the determining mechanism for ionic transport [4].

Ionic conductivity as a function of diffusivity, carrier concentrations and temperature can be obtained using the Nernst-Einstein relationship [3]:

$$\sigma = \sum_i \frac{q_i^2 \mathrm{F}^2}{k_\mathrm{B} T} c_i D_i, \tag{2.2.1}$$

where q_i is the charge of the carrier, F and k_B are the Faraday and Boltzmann constants, respectively, T is the absolute temperature (in Kelvin), c_i is the concentration of charge carriers (defects) and D_i is the diffusion coefficient (with a SI unit of $\frac{\mathrm{m}^2}{\mathrm{s}}$). The summation runs over all available types of charge carriers. It can be seen that the conductivity (σ) is influenced by two main factors, namely the diffusivity (D_i) and the carrier concentrations (c_i). The **diffusivity** (D_i) in solids , which represents the kinetic of the system, is described by means of an Arrhenius-type relationship as [3]:

$$D_i = D_0 e^{-\frac{\Delta E_\mathrm{M}^i}{k_\mathrm{B} T}}, \tag{2.2.2}$$

in which, D_0 is the exponential pre-factor (or maximal diffusion coefficient and is temperature independent) and ΔE_M^i represents the migration energy (diffusion energy barrier) of charge carriers (or defects). The **carrier concentrations** (c_i) is determined by the thermodynamic of the defects (as the charge carriers) which is represented by the defect formation energy (ΔE_F^i) and maximum concentration (c_0) as [3]:

$$c_i = c_0 e^{-\frac{\Delta E_\mathrm{F}^i}{k_\mathrm{B} T}}. \tag{2.2.3}$$

The activation energy, i.e. sum of the formation and migration energies of defects, can be obtained using *ab initio*-based calculations. This is where the defect formation energy

(Zhang-Northrup) equation for obtaining the $\Delta E_{\mathrm{F}}^{i}$ [94, 95] and transition state theory for formulating the $\Delta E_{\mathrm{M}}^{i}$ [96, 97] are employed.

In the following sections, first the methods for estimating the stability of surfaces and interfaces are discussed and then the approaches for calculations of defects formation and migration energies are explained.

2.2.1 Thermodynamics of Surfaces and Interfaces

In the first section of the results chapter, stability of the surfaces and interfaces in the case of crystalline Si surfaces and amorphous-Li_2Si/crystalline-Si interfaces are studied. Therefore, it is necessary to provide a short overview of the basic thermodynamics. As DFT only covers the microscopic scale while thermodynamic properties are normally classified in macroscopic scale, a general connection has to be established between them. Moreover, as it can also be seen from the Kohn-Sham formalisms, DFT is a zero-temperature and -pressure method for the calculation of the ground state energy. In the following section, it is explained how these two subjects can be linked.

The key concept to connect micro and macro scales in which the DFT output can be employed as the thermodynamic input is the **Gibbs free energy *(G)*** [98]:

$$G(T,P) = (E_{\mathrm{pot}} + E_{\mathrm{kin}}) - T(S_{\mathrm{vib}} + S_{\mathrm{config}}) + PV = U - TS + PV. \tag{2.2.4}$$

In this equation, E_{pot} is the potential energy (total energy) of the system with respect to its constituent nuclei and electrons in a steady state, E_{kin} is the kinetic energy of the system (sum of the vibrational, transitional and rotational energies of atoms or molecules in the system), T is the temperature and S_{vib}, S_{config}, P and V are vibrational and configurational entropy, pressure and volume, respectively. In a system which consists of n species, a change in the Gibbs free energy can be written as [98]:

$$dG = -SdT + VdP + \sum_{i=1}^{n} \mu_i dN_i, \tag{2.2.5}$$

in which, μ_i and N are the chemical potential and number of atoms for i^{th} species. If pressure and temperature are kept constant then the above equation is simplified to:

$$dG|_{T,P} = \sum_{i=1}^{n} \mu_i dN_i, \tag{2.2.6}$$

which shows that under these conditions, only a change in the chemical potential can lead to a change in Gibbs free energy of the system. If the system is in equilibrium,

which can exchange particles with its environment, the change in Gibbs free energy is zero ($dG = 0$), thus the following expression holds:

$$\sum_{i=1}^{n} \mu_i dN_i = 0. \tag{2.2.7}$$

Therefore, the chemical potential is given by:

$$\mu_i = \frac{\partial G}{\partial N}|_{T,P}. \tag{2.2.8}$$

So far, the properties related to bulk phases without any contributions from surfaces and/or interfaces are shown. Now it is explained how to deal with the thermodynamics of surfaces and interfaces. This is important because if we aim to study, for example, nanostructures, stability of surfaces and interfaces play an important role. Therefore, a description should be presented with which we could show whether or not a surface or an interface can be formed from thermodynamic point of view. To do so, the definition of **surface free energy**, which is obtained from the following equation, can be evaluated [98]:

$$\gamma_{\text{surface}}(T, P) = \frac{1}{2A}\Big[G_{\text{surface}}(T, P, N_i) - \sum_{i=1}^{n} \mu_i N_i(T, P)\Big]. \tag{2.2.9}$$

In this equation, G_{surface} is the Gibbs free energy of the surface (which can be modeled by a slab, see section 2.1.8) and μ_i is the chemical potential of i^{th} specie. N_i is the total number of atoms for the i^{th} specie. In this expression, γ_{surface} is normalized with respect to the surface area (A) of the slab model, thus it has the unit of energy per area. The 1/2 factor in Eq. 2.2.9 rises from the fact that the symmetric slab model has two identical sides. In case of asymmetric slabs, the value of surface free energy will be in fact the average of both surfaces. A smaller value of γ_{surface} shows more stability of that surface. Usually in the *ab initio* modeling of materials, it is common to use the DFT total energy instead of Gibbs free energy, since other contributions in Eq. 2.2.4 in case of solids can be disregarded, however, it is possible to introduce them as well. Therefore, Eq. 2.2.9 can also be written as:

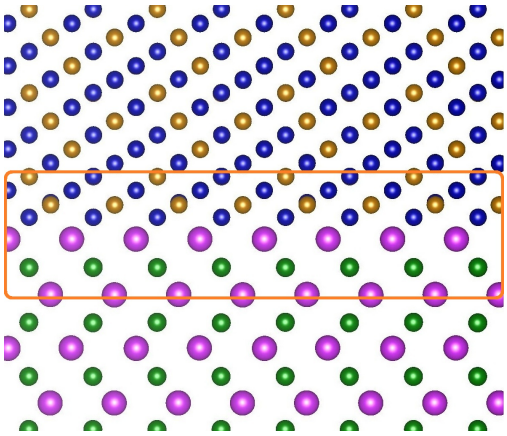

Figure 7: Example of an asymmetric interface in a metallic system. Interface region is indicated with a red rectangular.

$$\gamma_{\text{surface}} = \frac{1}{2A}\Big[E_{\text{surface}} - nE_{\text{bulk}}\Big]. \tag{2.2.10}$$

In Eq. 2.2.10, E_{surface} is the total energy of a slab model consisting of n unit formula and E_{bulk} is the total energy of bulk per unit formula. With the same procedure, the interface free energy (γ_{int}) (see Fig. 7) is also given using the equation below:

$$\gamma_{\text{int}} = \frac{1}{2A}\Big[E_{\text{int}} - n_1 E^a_{\text{bulk}} - n_2 E^b_{\text{bulk}}\Big]. \tag{2.2.11}$$

where E_{int} is the total energy of the interface model and E^a_{bulk} and E^b_{bulk} are the total energies of bulk materials where the surfaces are truncated from. Both Eqs. 2.2.10 and 2.2.11 can be applied for stoichiometric surfaces. In publication **A1**, stability of surfaces and interfaces using the presented approaches in this section are estimated.

2.2.2 Atomistic Thermodynamic: Defect Formation Energy

In the second section of the results chapter, i.e. publication **A2**, formation and migration of different types of defect (both in charged and neutral states) are evaluated. The discussion of defect migration is covered in section 2.2.3 while in this section it is first shown how to deal with the calculation of defect formation energy.

Formation energy of defects in a neutral system (supercell) can be calculated using the following equation [94, 95]

$$\Delta E^i_{\text{F}} = E^i_{\text{tot}} - E^{\text{pr}}_{\text{tot}} \pm \sum_i n_i \mu_i. \tag{2.2.12}$$

In this equation, E^i_{tot} and $E^{\text{pr}}_{\text{tot}}$ are the total energies of the defective and defect-free (pristine) systems, respectively. Also, n_i and μ_i are number and chemical potential of each defect type, respectively. The $\sum_i$ runs over all type of defects. Obtaining the ΔE^i_{F} using Eq. 2.2.12 for the neutral supercells is straight-forward, however, since in this thesis bulk Li_2S is modeled using periodic charged supercells as well, special procedures in this case must be considered due to the three following problems:

1. If the defects (more accurately, the supercells) would be charged, a neutralizing background charge (jellium) must be defined which makes the electrostatic energy per unit cell to be finite. Without this background charge, due to a strong charge-charge repulsion between two adjacent cells, the total energy calculation diverges and supercell collapses. As the result of the unphysical interactions between the charged defects in periodic cells (images) with each other and with the jellium background charge, an energy correction (E_{cor}) term has to be introduced in Eq. 2.2.12.

2. In charged-supercells calculations, the charge states of the pristine and defective systems are not the same. Therefore to have a proper description, the chemical potential of electrons (Fermi energy, ϵ_{F}) should be introduced in the Eq. 2.2.12.

3. The electrostatic potentials ($\Delta V_{q/0}$) of pristine and defective cells have to be aligned.

Thus, the general form of Eq. 2.2.12 is written as:

$$\Delta E_{\mathrm{F}}^{i,q} = E_{\mathrm{tot}}^{i,q} - E_{\mathrm{tot}}^{\mathrm{pr}} \pm \sum_i n_i \mu_i + q(\epsilon_{\mathrm{F}} + \epsilon_{\mathrm{VBM}} + \Delta V_{q/0}) + E_{\mathrm{cor}}. \tag{2.2.13}$$

In this equation, q, ϵ_F, ϵ_{VBM}, $\Delta V_{q/0}$ and E_{cor} are the charge of defects, Fermi energy, valence band minimum, potential alignment and the energy correction, respectively. The second problem is already addressed in Eq. 2.2.13 (with the fourth term). In order to tackle the first and third issues mentioned above, the method of correction developed by Freysoldt, Neugebauer and Van de Walle, referred to as **FNV** [99, 100], is briefly explained.

One of the drawbacks of the supercell approach is the finite unit cell size effect. This means that in the case of defective systems, an isolated defect in the bulk is in fact repeated infinitely in 3D and this causes the defect concentration to artificially and largely increases. Therefore, across adjacent cells, there is substantial interaction between defects, such as overlap of wavefunctions and strain fields (is discussed in section 2.3). If these defects have a positive or negative charge, electrostatic interaction will also be added to the mentioned defect-defect interactions. For the wavefunction and strain field overlap between two defects, the remedy is to increase the size of the supercell to minimize the undesired image-image interactions. In the case of electrostatic interactions, however, small increase in the cell size is not always the solution because both the long-range defect-defect interaction and the interaction between the charged defect and the background charge will not vanish easily, unless there would be special conditions such as being in the very dilute limit and/or extremely large supercells [48, 101]. Therefore for the calculation of the defect formation energy in charged state, a correction based on the FNV method is employed which is defined as:

$$E_{\mathrm{cor}}^{\mathrm{FNV}} = E_{\mathrm{latt}} - q\Delta V_{q/0}. \tag{2.2.14}$$

In this equation, E_{latt} for a point charge is equal to $\dfrac{q^2\alpha}{2\epsilon L}$ in which q, α, ϵ and L are the defect charge, Madelung constant (depends on the Bravais lattice), dielectric constant and linear dimension of the supercell, respectively. In the Eq. 2.2.14, $\Delta V_{q/0}$ is the potential

alignment term (see Eq. 2.2.13) and can be obtained using the following equation at a position far from the defect:

$$\Delta V_{q/0} = \frac{1}{\Omega}\int V_{\mathrm{sr}}(r)d^3r = (V_q^{\mathrm{DFT}} - V_0^{\mathrm{DFT}})|_{\mathrm{far}} - V^{\mathrm{model}}|_{\mathrm{far}}, \tag{2.2.15}$$

where V_q^{DFT}, V_0^{DFT} and V^{model} are the potentials of defect charge, neutral case and model charge, respectively. For localized defects, usually a Gaussian function with a small width is chosen as the model charge. However, as long as the defect charge is well localized within the supercell, regardless of the form of the model charge, a converged value for the $E_{\mathrm{cor}}^{\mathrm{FNV}}$ is obtained. Due to the presence of a defect in supercell, local effects which lead to differences between the DFT potential and the model potential appear. These effects are mostly considered in the FNV scheme via an energy term, which can be mainly disregarded if the model supercell is large enough (usually more than 10 Å).

In the second section of the results chapter, the above mentioned procedure is used to study the defect chemistry in bulk Li_2S (publication **A2**). An important fact that should be noted is that the FNV method is very sensitive to the values of Fermi energy (ϵ_{F}), valence band maximum (VBM) and dielectric constant (ϵ), therefore, the mentioned properties should be computed with great precision.

2.2.3 Atomistic Kinetic: Transition State Theory and Diffusion

Atoms in a crystal show thermal vibrations, which increase at elevated temperatures. However, not all of these vibrations will lead to successful **jumps** which contribute to charge transfer and hence chemical reactions. In fact, only a small number of these jumps will contribute to the total conductivity in solids. Therefore, a method should be applied so that the successful jumps can be distinguished from the others. **Transition state theory (TST)** solves this problem by excluding those successful contributing events from all other unimportant vibrations. Before going into more details, the concept of a **potential energy surface (PES)** is explained [103]. The mathematical description which expresses

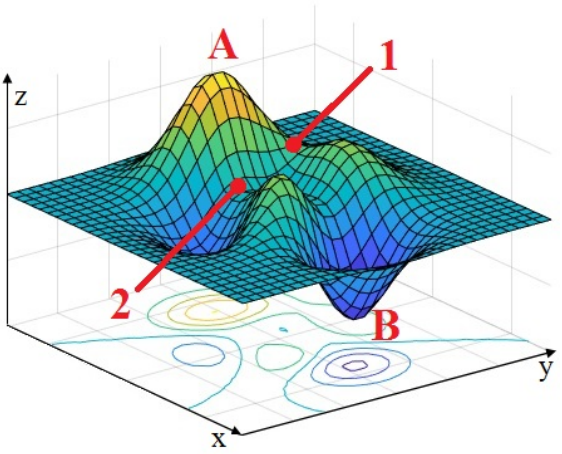

Figure 8: Example of a random potential energy surface adopted from Matlab database [102]. Points "A" and "B" show the global and local minima while solid circle points "1" and "2" indicate the saddle points, respectively.

the energy of a system of atoms as a function of their geometries ($E(\vec{r})$) is referred to as the potential energy surface (PES). This potential energy does not change in cases of translation and/or rotation of the system and it only depends on the internal coordinates of the atoms. Therefore, it depends on $3N-6$ coordinates, where three translations and three rotations are excluded (N is the number of atoms) [103]. In this representation which is similar to a topographical map, the status of the system is assumed to be similar to a small ball moving on this topography. If there is not enough energy, for example, at point "B" in Fig. 8 and the ball is expected to move towards point "1", it will permanently stay in **basin** "B" [97, 103, 104]. What TST in fact provides, is the estimation of the rate at which system is required to move from basin "B" towards point "1" at a fixed temperature. The effect of temperature is similar to kicking the ball. If the kick is strong enough, it will cause the ball to move forward [97, 103, 104]. Transition state theory can not be used to calculate the amount of energy which is needed to move a particle from one basin to another in case any *additional factor* such as temperature is involved [97, 103, 104]. Therefore, without considering the effect of temperature, the energy barrier, which the reaction needs to overcome, can be calculated using the following relationship:

$$\Delta E_{\mathrm{M}} = E_{\mathrm{tot}}^{\mathrm{S}} - E_{\mathrm{tot}}^{\mathrm{I}}, \tag{2.2.16}$$

where $E_{\mathrm{tot}}^{\mathrm{S}}$ is the total energy of the system in the saddle point (or transition state, e.g. point "1" in Fig. 8) and $E_{\mathrm{tot}}^{\mathrm{I}}$ is the total energy in the initial state (e.g. point "B" in Fig. 8). As it can be seen from Fig. 8, finding the correct path and transition point between two basins with minimum energies is not a trivial task since there could be many ways to move from the initial to the final state [105].

One common technique for finding the diffusion mechanism and pathway is called the **nudge elastic band (NEB)** method [97, 104]. In the NEB method, the whole reaction path is established between the initial and the final states. In this method, a string of **images** between initial and final states is created. For these images, one spring between successive points is assumed to keep the distance between the images equally fixed [97, 104]. Thus, it acts similar to an elastic band. All these images receive two sources of force, one from the hypothetical spring between them and one due to the potential energy acting on them, which they try to minimize. The nudging (force projection) approach is then divided into two parts, one along the images (band) coming from the spring and the other on the images from the potential energy in all directions perpendicular to the path [97, 104].

In some cases where the normal NEB method fails to point out the true saddle point, a modified NEB may be applied. This scheme is called **climbing nudge elastic band (Cl-NEB)**. In this method, the shape of the minimum energy path is conserved and other images help to find the reaction coordinates around the saddle point. By converging the energies in the Cl-NEB method, the image with the highest energy will converge to the energy of the saddle point. Fig. 9 (from reference [97]) shows the difference between the regular and climbing NEB schemes. In Fig. 9, the dissociated H^+ and CH_3^- radicals on a top-site position over Ir(111) surface and CH_4 molecule with 4 $\mathring{A}$ distance from the Ir(111) surface correspond to 0.0 and 1.0 reaction coordinates, respectively. Since the number of images in both methods are the same and equal to 8 (first and last points are the initial and final state), the reaction coordinates and pathways are the same. However, since in the Cl-NEB method one image is shifted to the right side of the saddle point, it actually shows the transition state much more precisely [97].

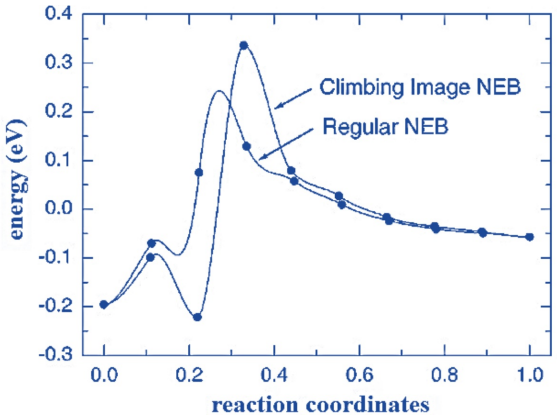

Figure 9: Comparison between NEB and Cl-NEB methods for the dissociation of CH_4 on Ir(111) surface from reference [97]. The NEB method results in a lower energy barrier due to the inaccurate saddle point.

Both NEB and Cl-NEB methods are implemented in most DFT-codes. In this thesis and within all publications, the calculations for determining the energy barrier of Li and hole-polaron migrations are performed using both NEB (as the initial step) and Cl-NEB (as the complementary step) implemented in `VASP` and `SeqQuest`.

2.3 Effect of Stress/Strain on Conductivity

2.3.1 Stress/Strain Relationship

The mechanical definition of **stress** (σ) is the applied force over a specific area ($\sigma = \frac{F}{A}$ with the SI unit of $\frac{N}{m^2}$). From the atomistic point of view, stress is referred to as the interatomic forces, which are transferred between atomic species, per unit area and are eventually applied to the unit cell (or supercell) boundaries. Fig. 10-a shows a schematic view of the general definition of stress. Three main forms of stress are compression, tension and shear as shown in Fig. 10-b. Usually in battery materials, the appearance of the first two

types of stress is more common. When any type of stress is applied to a material, depending on its **elastic modulus** (also called Young's modulus or tensile modulus), a certain amount of strain appears in that material. If this stress (or strain) does not exceed a certain limit so that the material is not permanently deformed, i.e. the material stays in the reversible elastic regime and will return to its initial shape when the stress is removed, the following relationship for a uniaxial stress will be established as [106, 107]:

$$E = \frac{\sigma}{\epsilon}, \tag{2.3.1}$$

where elastic modulus (E) and stress (σ) have the same unit of pressure (e.g. Pa), thus strain (ϵ) is a dimensionless property and is defined as:

$$\epsilon = \frac{dl}{l_0}, \tag{2.3.2}$$

in which dl is the change in length and l_0 is the initial dimension. Stress/strain, similar to most of the materials properties, are direction dependent, thus they cannot be expressed as scalars but have to be dealt with in the form of tensors. Generally stress/strain can be shown in a second-rank tensor with 9 components and if they can be mapped in a space where all the points can be corresponded to a specific component of stress/strain, they are also referred to as **stress/strain fields** [108].

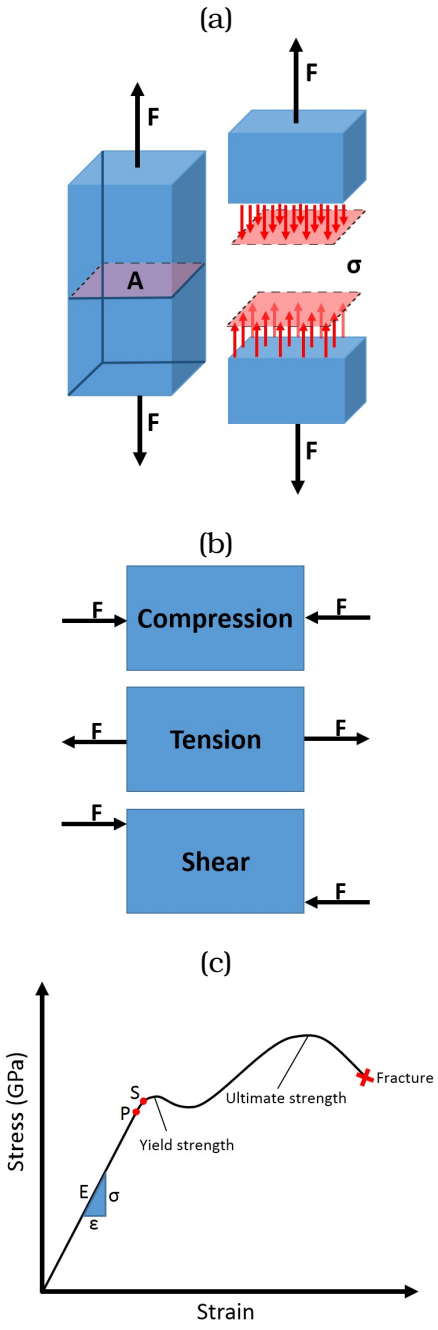

Figure 10: (a) Schematic of applied force at the cross-section and the resulted stress. (b) Schematic of three different types of stress. (c) Stress/strain plot for a ductile material [106, 107].

Fig. 10-c shows the deformation of a ductile system as a function of an uniaxial load. This plot consists of several zones. The first part, from the origin up to the point P, is the linear elastic region where stress and strain are proportional to each other and Eq. 2.3.1 is applied. From point P to S is referred to as the non-linear elastic region. Beyond point S,

if the load on material is removed, it will not return back to its original shape. The maximum load that a material can tolerate before permanently entering the plastic region is called the yield strength. From point S to fracture point is the plastic region where the corresponding load causes permanent deformation to the material. Ultimate strength is the maximum amount of load that a material can tolerate before it breaks. In battery materials, the generated stress/strain during the lithiation/delithiation processes should be in the elastic region (up to the point S), otherwise, destruction of the battery is expected.

The stress/strain relationship in the elastic region for a continuous medium obeys the Hook's law. In the Hook's law, the force and displacement of a spring are related through a **spring constant (*k*)**. In a continuous medium, it is also established that the applied stress and generated strain are related through the **elastic constants** or **stiffness tensor (*c*)**. Opposite to the case of a spring where k is defined by a one-dimensional vector, c for a material is described by a fourth-order tensor. The continuous form of Eq. 2.3.1 in the elastic region is then expressed by [106, 107]:

$$\sigma_{ij} = \sum_{k=1}^{3}\sum_{l=1}^{3} c_{ijkl}\epsilon_{kl} \quad \text{with} \quad i \,\&\, j = 1,\ 2,\ 3. \tag{2.3.3}$$

In this equation, stress (σ_{ij}) and strain (ϵ_{kl}) are second-order tensors. In general, the stiffness tensor (c_{ijkl}) is represented by a tensor with 81 components and due to the symmetry of crystals, the number of these components can be reduced. For example in the case of hexagonal systems (e.g. in $LiCoO_2$), full elastic constants are defined by only five independent components (namely, $c_{11}, c_{12}, c_{13}, c_{33}, c_{55}$, shown with Voigt notation). Finally, The change in the energy of a system due to the applied strain, which is referred to as the **elastic energy**, is given by [106, 107]:

$$E(V,\epsilon) = E(V_0,0) + \frac{1}{2}V_0\Big(\sum_{\alpha\beta} c_{\alpha\beta}\epsilon_\alpha\epsilon_\beta\Big), \tag{2.3.4}$$

where ϵ_α and ϵ_β are second-order strain tensors and V_0 is the initial volume. The elastic energy ($E(V,\epsilon)$ in Eq. 2.3.4) is in fact the area under the curve of Fig. 10-c within the linear elastic region.

2.3.2 Elastic Dipole Tensor

Creation of point defects causes two phenomena. The first one is a short-range local distortion (strain) around the defect site and the second one is a long-range **lattice distortion**. The latter induces changes in the cell parameters which result in a volume

change, called "**formation volume**". One theoretical approach to calculate the formation volume is using the concept of "**elastic dipole tensor (*G*)**". The name comes from the analogy of the interaction between an electric field and electric dipole moment. Here, the interaction is between a strain field and a defect. For the calculation of the elastic dipole tensor, Taylor expansion of the free energy per unit volume and density of defects (n_{d}) is considered. By disregarding the entropy contributions at 0 K, the following expression is established [109, 110, 111]:

$$\begin{aligned} E(n_d, \epsilon_{ij}) =& E^{\mathrm{p}} \pm n_{\mathrm{d}}\mu_{\mathrm{d}} + \frac{\partial E}{\partial n_{\mathrm{d}}} n_{\mathrm{d}} + \frac{1}{2}\frac{\partial^2 E}{\partial n_{\mathrm{d}}^2} n_{\mathrm{d}}^2 + \ldots + \sum_{i,j} \underbrace{\frac{\partial E}{\partial \epsilon_{ij}}}_{\sigma_{ij}\approx 0} \epsilon_{ij} \\ &+ \frac{1}{2}\sum_{i,j} \frac{\partial^2 E}{\partial \epsilon_{ij}\partial \epsilon_{kl}} \epsilon_{ij}\epsilon_{kl} + \ldots + \sum_{i,j} \frac{\partial^2 E}{\partial n_{\mathrm{d}}\partial \epsilon_{ij}} \epsilon_{ij} n_{\mathrm{d}}. \end{aligned} \tag{2.3.5}$$

In this equation, E^{p} is the total energy of the strain- and defect-free system, μ_{d} is the chemical potential of defect, $\dfrac{\partial E}{\partial n_{\mathrm{d}}} = \Delta E_{\mathrm{F}}$ is the strain-free defect formation energy, $\dfrac{\partial^2 E}{\partial n_{\mathrm{d}}^2} = E_{\mathrm{dd}}$ is the strain-free interaction energy between two defects, $\dfrac{\partial E}{\partial \epsilon_{ij}} = \sigma_{ij}$ is the stress of the system and vanishes in the absence of a defect, $\dfrac{\partial^2 E}{\partial \epsilon_{ij}\partial \epsilon_{kl}} = c_{ijkl}$ is the stiffness tensor of the material and finally $\dfrac{\partial^2 E}{\partial n_{\mathrm{d}}\partial \epsilon_{ij}} = \dfrac{\partial \sigma_{ij}}{\partial n_{\mathrm{d}}} = -G_{ij}$ is the elastic dipole tensor. Therefore, it can be seen that G_{ij} describes the interaction of a defect with a strain field and depends on the density of defects.

To calculate the elastic dipole tensor in this thesis, the **strain-controlled** method is used where the first derivative of $E(n_{\mathrm{d}}, \epsilon_{ij})$ (from Eq. 2.3.5) with respect to a fixed strain is considered:

$$\sigma_{ij} \equiv \frac{\partial E(n_{\mathrm{d}}, \epsilon_{ij})}{\partial \epsilon_{ij}} = \sum_{kl} C_{ijkl}\epsilon_{kl} - n_{\mathrm{d}} G_{ij} = \sigma_{ij}^0 - n_{\mathrm{d}} G_{ij}. \tag{2.3.6}$$

For a given supercell and density of defects, the elastic dipole tensor can then be calculated using the following equation [109, 110, 111]:

$$G_{ij} = -\left.\frac{\partial \sigma_{ij}}{\partial n_{\mathrm{d}}}\right|_{\epsilon_{ij}} = -\frac{1}{n_{\mathrm{d}}}(\sigma_{ij}^{\mathrm{d}} - \sigma_{ij}^0) = -V_0 \Delta \sigma_{ij}^{\mathrm{d}}, \tag{2.3.7}$$

in which V_0 is the volume of the supercell, σ_{ij}^{d} is the stress of the defected cell and σ_{ij}^0 is the stress of the defect-free cell (which is almost equal to zero). An important result obtained from this description is the change in the energy due to the interaction between a defect and applied external strain (disregarding the bulk contributions) by means of G_{ij} which can be written as [109, 110, 111]:

$$\Delta E = -\sum_{ij} G_{ij}\epsilon_{ij} = -tr(G \cdot \epsilon). \tag{2.3.8}$$

This equation can then be used to reformulate the previous equation for the calculation of diffusion energy barrier (ΔE_{M}) in the presence of strain. By referring to Eq. 2.2.16:

$$\Delta E_{\mathrm{M}} = E^{\mathrm{S}}_{\mathrm{tot}} - E^{\mathrm{I}}_{\mathrm{tot}},$$

$E^{\mathrm{S}}_{\mathrm{tot}}$ is the total energy of the system in the saddle point and $E^{\mathrm{I}}_{\mathrm{tot}}$ is the total energy in the initial state. For a system under strain, the energy barrier can be calculated using one of the following approaches:
(1) Direct evaluation by applying a particular strain to the simulation cell, recalculating the total energies for the two states with the new cell geometries and using Eq. 2.2.16 or,
(2) Using Eq. 2.3.8 to reformulate Eq. 2.2.16 as the following form [112]:

$$\begin{aligned} \Delta E_{\mathrm{M}}(\epsilon_{ij}) &= \Delta E_{\mathrm{M}}(\epsilon = 0) + \Delta E = [E^{\mathrm{S}}_{\mathrm{tot}} - E^{\mathrm{I}}_{\mathrm{tot}}] - [G^{\mathrm{S}}_{ij}\epsilon_{ij} - G^{\mathrm{I}}_{ij}\epsilon_{ij}] \\ &= \Delta E_{\mathrm{M}}(\epsilon = 0) - \Delta G^{\mathrm{M}}_{ij}\epsilon_{ij}. \end{aligned} \tag{2.3.9}$$

The second approach is computationally much more efficient, especially if there is a complicated strain field involved since there are only a few DFT calculations are needed: First, the energy barrier for the unstrained case using NEB method has to be calculated ($\Delta E_{\mathrm{M}}(\epsilon = 0)$). Second, using the coordinates obtained from the NEB calculation of the unstrained case, elastic dipole tensor at initial and transition state is computed and finally using Eq. 2.3.9 we can analytically predict the variation of energy barrier as a function of strain.

The formation energy of defects as a function of strain can also be predicted using this approach. The strain-free equation for the calculation of defect formation energy (Eq. 2.2.13 from section 2.2.2) is reminded:

$$\Delta E^{i,q}_{\mathrm{F}}(\epsilon = 0) = E^{i,q}_{\mathrm{tot}}(\epsilon = 0) - E^{\mathrm{pr}}_{\mathrm{tot}}(\epsilon = 0) \pm \sum_i n_i\mu_i + q(\epsilon_f + \epsilon_{VBM} + \Delta V_{q,0}) + E^{\mathrm{FNV}}_{\mathrm{cor}}.$$

Considering Eq. 2.3.8, Eq. 2.2.13 for the strained case can be written as the following form:

$$\Delta E^{i,q}_{\mathrm{F}}(\epsilon) = \Delta E^{i,q}_{\mathrm{F}}(\epsilon = 0) - n_d \sum_{ij} G_{ij}\epsilon_{ij}. \tag{2.3.10}$$

To sum up, it is demonstrated how using the elastic dipole tensor (EDT) method, computationally demanding calculations for the coupling between applied external strain and defect formation and migration energies can be evaluated. In the publications **A4** and **A5**, the EDT method is employed to first obtain the G_{ij} and afterwards to estimate the influence of strain on conductivity of the charge carriers in bulk $LiCoO_2$.

2.4 Electronic Conductivity

The origin of electronic conductivity in materials is diverse and system-dependent. In metals, according to the Drude's model, the electronic conductivity is assumed as a classical pinball model and caused by the constant movements of the "electrons sea" which hits and bounces off the heavy immobile particles (positive ions) [113]. In intrinsic semiconductors, since the number of free electrons is much smaller than metals, they are generally poor electronic conductors. The position of the Fermi level in intrinsic semiconductors lies in the middle of the band gap. Nevertheless, their electronic conductivity can increase by adding certain impurities, which turns them into extrinsic semiconductors, or by increasing the temperature. In fact, by doping intrinsic semiconductors with impurities (either n- or p-type), electrons may be added to conduction band or holes to valence band, respectively (see Fig. 11) [114].

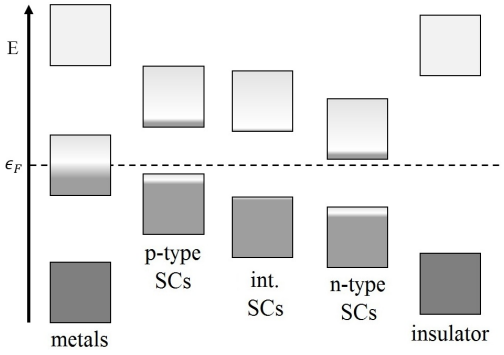

Figure 11: Schematic of band filling for different types of materials. From left to right, metals, p-type, intrinsic and n-type semiconductors and insulators are shown.

In the case of highly polar semiconductors, when a dopant (e.g. electron donor) is introduced in a crystal, it interacts with the positive and negative ions in the structure of the host material. Consequently, due to the Coulomb interactions, the extra electrons coming from the dopant will *locally* polarize the host material in such a way that positive ions are attracted to the extra electrons while negative ions are repelled from them. Therefore, the introduced electrons are surrounded by a cloud of **virtual phonon** as a result of such polarization. The combination of one electron and its virtual phonon is called a **polaron** (together are referred to as electron-polaron) [49, 50]. Depending on the size of the polarization cloud, being smaller or larger than the structural units, "small or large polarons" are defined [49, 50].

In the present thesis, the polaron formation is investigated in bulk-$LiCoO_2$ which is a highly polar semiconductor. In materials such as $LiCoO_2$, due to the strong electron-lattice coupling, immobilization of charge carrier (electron- or hole-polaron) occurs. In fact, the very slow movement of electron (or hole) through the ions leads to ionic displacements and creation of a potential well and eventually results in the trapping of polaron in this potential well. This temporary immobilization is called **self-trapped** and under certain condition (i.e. providing the required energy barrier) electron- (or hole-)

polaron can jump from one self-trapped state to another [49]. It should be noted that in spite of the fact that the generated strain due to the atomic displacements can be energetically unfavorable for the system, the self-trapped condition causes a reduction in the total energy and makes it energetically more favorable (compared to the case where the particle is not self-trapped). The concept of self-trapped small polarons is very helpful in materials modeling since it can be employed to predict the electronic conductivity of semiconductors.

Before the details of polaron hopping are explained, which can eventually be used to calculate the electronic conductivity, two main mechanisms of charge transfer, namely **adiabatic and non-adiabatic** shown in Figs. 12-a to 12-c, are discussed. Fig. 12-a shows the system in two states. State A shows that electron-polaron is localized on the left molecule and state B shows the system after electron-polaron transfers [50, 115, 117]. The difference between these two mechanisms is related to the form an electron hops between the two states. In the adiabatic process, the electron transfers smoothly and without any quantum jump. In the diabatic process, however, electron hops from one state to the excited state and after oscillation, it may jump to either side, depending on the energy barrier. In Fig. 12-b, the dashed curve between the two states shows the adiabatic transfer resulting from the overlap of the two states. $\Delta E_{\mathrm{M}}^{\mathrm{p}}$ is the energy barrier of electron (or hole) hopping and t is the transfer integral (electron coupling) which is a measure for the degree of the orbitals overlap. In the adiabatic process, the transfer integral decreases the energy barrier and results in a successful electron transfer. During this process, the oxidation state of the central atom,

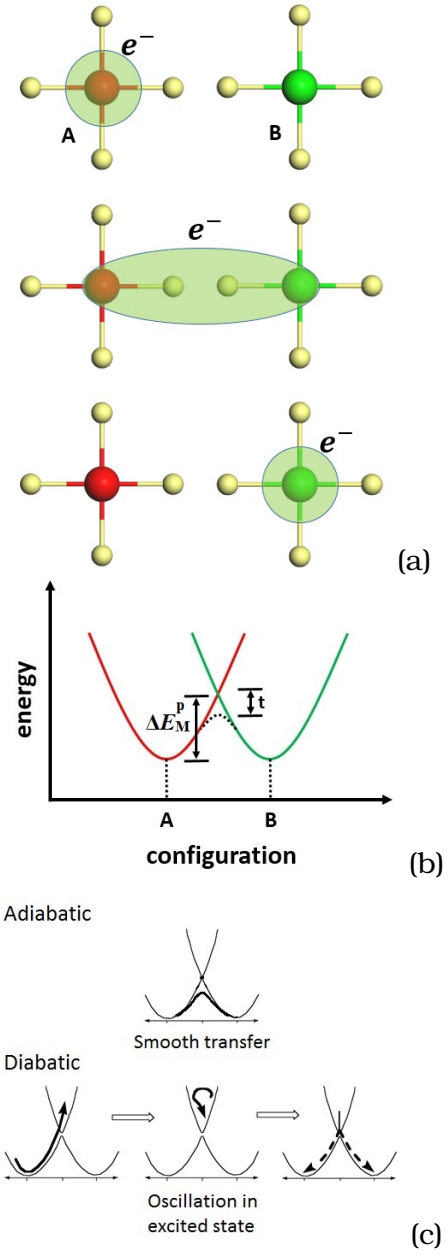

Figure 12: (a) Schematic of polaron hopping between two molecules A and B. (b) Corresponding energy profile for electron-polaron transfer for the same species of part (a). (c) Mechanisms of adiabatic and non-adiabatic (diabatic) charge transfer [49, 115, 116].

where electron-polaron is formed, changes. Due to the absence of excited state and the mentioned smooth transfer of electron-polaron, the transition state theory within the framework of the DFT in the case of adiabatic process can be employed. In other words, NEB method can be utilized to determine the migration energy of the adiabatic process [49, 50, 117].

After the energy barrier for the electron- or hole-polaron migration is determined, using the following equation, electronic conductivity can be calculated for most of the semiconductors:

$$\sigma = ne\mu_d(T), \tag{2.4.1}$$

where n is the concentration of electrons (or holes), e is the charge of an electron and $\mu_d(T)$ is the electron (or hole) temperature-dependent mobility. To calculate the mobility of electron- or hole-polaron in the adiabatic regime, the following Arrhenius equation is used:

$$\mu_d(T) = \left[\frac{ega^2\nu_0}{k_BT}\right] exp\left(\frac{-\Delta E_{\mathrm{M}}^{\mathrm{p}}}{k_BT}\right), \tag{2.4.2}$$

in which, a, g, ν_0 and k_B are the hopping distance, geometric factor determined by vector analysis, characteristic phonon frequency and Boltzmann constant, respectively. T and $\Delta E_{\mathrm{M}}^{\mathrm{p}}$ are temperature and polaron hopping energy barrier.

The above method is employed in the publication **A5** in order to estimate the electronic conductivity in bulk $LiCoO_2$. In addition, coupling between stress/strain and migration of polaronic defect is performed using the elastic dipole tensor method.

3 Results and Publications

In this chapter, after literature review and summary of the results, **five publications** within the context of "charge transport in Li-based batteries" are provided. The results presented in this chapter are categorized into the following three main sections:

1. Lithiation of silicon (**A1**),
2. Defect chemistry in Li_2S (**A2**),
3. Mechanism of Li diffusion in bulk and the most stable surface of $LiCoO_2$ as well as investigation of the effect of stress/strain on the ionic and electronic transport in bulk $LiCoO_2$ using the concept of "elastic dipole tensor" (**A3, A4 and A5**).

3.1 Literature Review

Publication A1

In the previous studies, lithiation of (111) and (100) surfaces of c-Si [118, 119], as well as amorphous bulk [120, 121], Li-Si alloy [23, 122] and nanostructures of silicon [123, 124] have been investigated. My colleagues, Rohrer *et al.*, in a theoretical study have shown that the lithiation of c-Si results in the formation of a two-phase model consisting of c-Si/a-Li_2Si [23]. Formation of Li_2Si is in agreement with the work of Kim *et al.* [122]. In a study by Chan *et al.* [125], lithiation of c-Si and formation of Li_xSi phase using density functional theory calculations have been reported. However, due to the small size of their model, the amorphous nature and stoichiometry of Li_xSi can not be correctly evaluated.

Publication A2

A study of defect chemistry using *ab initio*-based calculations in Li_2S has not been performed so far. In a comprehensive experimental study, Xu *et al.* have reported the formation of Li_2S around S_8 molecule as a two-phase shell/core structure [19]. They have shown that the formation of Li_2S as a crust around S_8 will hinder further lithiation of sulfur. Yang *et al.* have discussed the decrease in discharge capacity in Li-S batteries due to the formation of solid Li_2S and Li_2S_2 precipitation on the cathode side [20]. Both these studies imply the low ionic conductivity in Li_2S.

Publications A3-A5

In several experimental and theoretical studies, the phase stability in bulk [126], formation and stability of different surfaces [127] and Li migration in bulk and thin films of $LiCoO_2$ (LCO) [128, 129] have been reported. However, lithiation/delithiation of LCO at its most stable surfaces, effects of the magnetic and non-magnetic defect states as well as DFT functional corrected with an onsite Hubbard term for Co on Li migration and effect of stress/strain on the electronic and ionic conductivity of LCO have not been deeply investigated so far. Li diffusion in bulk-LCO has already been investigated using DFT calculations in the study by Van der Ven *et al.* [128], however in their work, magnetic properties of LCO upon lithiation/delithiation and effect of spin polarization and XC functionals on migration energy barrier of Li have not been discussed. Moreover, Kramer *et al.* using theoretical methods have investigated various surfaces of LCO-nanoparticles and found that in a reasonable chemical potential range of Li and O, (0001) and $(10\bar{1}4)$ surfaces are the most stable ones [127]. However, based on its crystal structure, only the $(10\bar{1}4)$ surface of LCO is active for Li migration which is not investigated so far.
The effect of strain on Li ion migration in bulk-LCO has been studied by Ning *et al.* [130]. They have shown that Li ion migration barrier decreases significantly when tensile stress is applied along the c-axis direction and changes the diffusion coefficient by several orders of magnitude at room temperature. However, they have only employed the conventional method (NEB at each strain regime) which is computationally demanding. Although, they have not discussed the effect of strain on the defect formation and hence the total activation energy. Electronic conductivity of LCO and effect of strain on it have also not been studied so far.

3.2 Summary of the Results

By using silicon nanostructures, it is feasible to greatly overcome the problem of low mechanical stability in silicon anodes during the lithiation process [30, 32]. Lithiation of crystalline silicon nanowires (c-Si) is initially accompanied by the formation of amorphous Li_2Si (a-Li_2Si) which leads to the existence of a core/shell two-phase structure. Further lithiation of c-Si takes place through the movements of a-Li_2Si/c-Si interfaces. Further studies indicated that in silicon nanowires, an anisotropic expansion occurs at the interfaces of the mentioned core/shell structure during further lithiation process which is orientation dependent (see Fig. 3 in chapter 1) [26, 33, 34]. The origin of this

orientation dependent mobility of interfaces which can eventually lead to the deformation of silicon nanowires is not well understood. In publication **A1**, using density functional theory calculations, first the lithiation of the three most stable surfaces of crystalline silicon (c-Si) is studied. It is found that the Li adsorption initially starts on the (110) surface of clean c-Si. The minimum energy barrier for the Li diffusion also belongs to the (110) surface at high Li concentration. Afterwards, by creating an explicit two-phase core/shell model with c-Si as core and a-Li_2Si as shell, thermodynamic and kinetic of the further lithiation of silicon nanowires are evaluated [35]. Results show that the origin of the orientation-dependent lithiation of silicon nanowires is not due to a faster Li diffusion at the interfaces of a-Li_2Si/c-Si but rather is the consequence of various interface formation energies. It is shown that since a-Li_2Si/c-Si(110) interface has the highest formation energy among the others, it is less stable, i.e. more mobile, and therefore the growth of silicon nanowire during the lithiation process occurs faster along (110) direction. It is also revealed that the values of the energy barrier for Li migration at all of the three interfaces, opposite to their corresponding c-Si surfaces, are non-uniformly distributed which is related to the amorphous nature of Li_2Si phase.

In the publication **A2**, defect chemistry and various mechanisms of 3D Li diffusion in Li_2S using density functional theory calculations together with thermodynamic and kinetic considerations are investigated [22]. The aim is to unveil the origin of the low ionic conductivity in Li_2S which has been observed in experiments [16, 17, 19]. In this study, calculated formation energies of all possible defect types in Li_2S as a function of the chemical potential of Li (or cell voltage) are plotted. Using the defect stability diagram, it is found that the most stable defect type in Li_2S is a Frenkel pair (combination of a charged vacancy and interstitial) with a very high formation energy of about 2.2 eV. The most favorable migration mechanism is conducted by a single Li vacancy hopping with the energy barrier of 0.27 eV, while the energy barrier of the exchange mechanism (via interstitial Li) is found to be 0.45 eV. As a result, the high activation energy for Li transport, i.e. $\Delta H_i = 1.42$ eV which is the sum of the formation and migration energies of a single Li vacancy, explains the reason behind the low ionic conductivity in Li_2S.

In the third section of the results chapter, ionic and electronic migration together with the effect of stress on the charge carriers mobilities in $LiCoO_2$ cathode material are investigated. At first in the publication **A3**, the mechanisms of Li diffusion in bulk and the most stable and diffusion-active, i.e. $(10\bar{1}4)$ surface, of $LiCoO_2$ are studied [24]. Moreover, the effect of using the PBE and PBE+U XC functionals as well as spin polarization

are investigated. Results reveal that the most favorable Li diffusion mechanism in both bulk and $(10\bar{1}4)$ surface of $LiCoO_2$ is the hopping of Li ions into a divacancy of lithium on a curved pathway. It is observed that the spin polarization does not significantly affect the Li migration energy. Furthermore, it is demonstrated that the PBE+U XC functional provides contributions of both ionic and polaronic diffusion energy barriers. It is shown that the Li diffusion on the topmost layer of $(10\bar{1}4)$ surface due to a weaker Co-O bonding takes place with almost zero energy barrier. However, by moving deeper into the layers of $(10\bar{1}4)$ surface, the Li migration energy increases.

As the last part of the results chapter, in publications **A4** and **A5**, the effect of stress/strain on the ionic and electronic conductivity in bulk $LiCoO_2$ is discussed using DFT calculations together with the computationally efficient "**elastic dipole tensor**" approach [48, 51]. As the first step and in the publication **A4**, the unit cell size dependence of the elastic dipole tensor in bulk $LiCoO_2$ is investigated. It is shown that there is a massive unit cell size effect for the computation of elastic dipole tensor in the dilute limit of defect concentration. However, a uniform lattice extension towards the dilute limit can result in a minimum coupling between the lateral and longitudinal components of stress which leads to minimization of the unit cell size effect. Furthermore, effect of strain on both formation and migration of Li vacancy with a specific concentration is estimated. It is observed that the impact of strain on migration energy is dominant and opposite of that on the formation energy. Moreover, it is revealed that the effect of stress on the ionic conductivity in bulk $LiCoO_2$ is significant. It is shown that by only 1% lateral tensile strain, up to about 3 times increase in the ionic diffusivity and hence the conductivity can be achieved. Effect of longitudinal strain on conductivity is even stronger.

In the publication **A5**, the electronic conductivity in bulk-$Li_{0.98}CoO_2$ using the small hole-polaron hopping concept is estimated at 300 K to be 2.3-2.7$\times$ 10^{-4} which is in agreement with experimental values of 1.0-3.3$\times 10^{-4}$ [131, 132]. The effect of strain on the electronic conductivity (polaron hopping) is also found to be significant but it is less pronounced than that of the ionic one. It is proved that the elastic dipole tensor method for studying the effect of strain on conductivity can be used for both cases, i.e. electronic and ionic transports. In general, it is shown that independent of the type of the defect, in any system with defect-induced stress, EDT method can be applied. The obtained results using this method for both cases are in good agreement with the conventional computationally-expensive method where the energy variations for each strain regime should be computed separately.

3.3 Contributions in the Publications

In the first publication **(A1)**, I was the second author and responsible for all the DFT calculations and analysis of structures, formation and migration energies at crystalline Si surfaces as well as a-Li_2Si/c-Si interfaces. The amorphous Li_2Si was modeled by my colleague, Dr. Rohrer, using DFT calculations in his previous work [23]. The atomic structures of the crystalline silicon were prepared by me and the interfaces were constructed by Dr. Rohrer and then were given to me. In this manuscript, Figs. 1 to 4 and table 1 were prepared by me and Figs. 5 and 6 by Dr. Rohrer. The idea of this work belongs to Dr. Kaghazchi, Dr. Rohrer and Prof. Albe. The writing task was conducted by Dr. Kaghazchi and Dr. Rohrer and commented by me and Prof. Albe.

The DFT calculations and preparation of figures and tables for the second and third publications **(A2** and **A3)** were completely conducted by me. The data analysis and interpretation of the results were conducted by both me and Dr. Kaghazchi. The idea of both works belongs to Dr. Kaghazchi. The writing task of both manuscripts were performed mainly by him and partly by me.

The forth publication **(A4)** is a joint research. The idea belongs to Prof. Albe. It is fully conducted and written by me at TU Darmstadt. Prof. Albe edited this manuscript and Dr. Rohrer and Dr. Kaghazchi commented on it. In this work, Dr. Rohrer and Dr. Kaghazchi also helped me with scientific discussions. At the time this thesis is being submitted, publication **(A4)** was already reviewed by the referees and minor revisions are requested. DFT calculations related to their comments are now being performed and the new results will be added to the resubmitted version.

The idea of the fifth publication **(A5)** was proposed by Dr. Kaghazchi. It was completely performed and prepared by me and he helped me with scientific discussions and data analysis. This publication was written both by me and him.

Section I:

– Lithiation of silicon

3.4 Publication A1

"On the origin of anisotropic lithiation of silicon"

Jochen Rohrer, Ashkan Moradabadi, Karsten Albe and Payam Kaghazchi

Journal of Power Sources 293 (2015), pp. 221-227.

DOI: 10.1016/j.jpowsour.2015.05.057
URL: http://doi.org/10.1016/j.jpowsour.2015.05.057

Section II:

– Defect chemistry in Li_2S

3.5 Publication A2

"Thermodynamics and kinetics of defects in Li_2S"

Ashkan Moradabadi and Payam Kaghazchi

Applied Physics Letters 108 (2016), p. 213906.

DOI: 10.1063/1.4952434
URL: http://dx.doi.org/10.1063/1.4952434

Section III:

– Li diffusion in bulk and the most stable surface of $LiCoO_2$

– Effect of strain on the ionic and electronic transport in bulk $LiCoO_2$

3.6 Publication A3

"Mechanism of Li intercalation/deintercalation into/from the surface of $LiCoO_2$"

Ashkan Moradabadi and Payam Kaghazchi

Physical Chemistry Chemical Physics 17 (2015), pp. 22917-22922.

DOI: 10.1039/c5cp02246k
URL: https://dx.doi.org/10.1039/C5CP02246K

3.7 Publication A4

"Influence of elastic strain on the thermodynamics and kinetics of lithium vacancy in bulk $LiCoO_2$"

Ashkan Moradabadi, Payam Kaghazchi, Jochen Rohrer and Karsten Albe

Submitted to *Physical Review Materials* in June 2017. Requested for minor revision
URL: https://arxiv.org/abs/1706.01709

3.8 Publication A5

"Effect of strain on polaron hopping and electronic conductivity in bulk $LiCoO_2$"

Ashkan Moradabadi and Payam Kaghazchi

Physical Review Applied 7 (2017), p. 064008.

DOI: 10.1103/PhysRevApplied.7.064008
URL: https://doi.org/10.1103/PhysRevApplied.7.064008

4 Conclusion and Outlook

In this thesis, I employed density functional theory calculations in conjunction with thermodynamic and kinetic considerations to study mechanisms of charge transport and conductivity in selected electrode materials for Li-ion batteries.
This dissertation consists of the following three different types of ionic migration: **i.** 3D Li diffusion accompanied by chemical reactions in the case of Si anode (publication **A1**), **ii.** 3D Li diffusion in low defect concentration without chemical reactions in the case of Li_2S cathode (publication **A2**) as well as **iii.** 2D Li diffusion in the dilute limit of defects concentration without chemical reactions in the case of $LiCoO_2$ cathode (publication **A3**). The concept of elastic dipole tensor (G_{ij}) and the effect of finite unit cell size on the computation of G_{ij} in the dilute limit were explored in bulk-$LiCoO_2$ (publication **A4**). Electronic conductivity via hole-polaron migration was computed in bulk $LiCoO_2$ using the concept of self-trapped small polarons (publication **A5**). In addition, the effect of stress/strain on both ionic and electronic conductivities were explored in bulk-$LiCoO_2$ using the elastic dipole tensor method (publications **A4-A5**).

In the publication **A1**, the origin of the experimentally reported anisotropic expansion of silicon nanowires during the lithiation process was evaluated. In order to accomplish this, thermodynamic and kinetic of Li migration at the surfaces of crystalline Si and at the interfaces of an explicit two phase model between crystalline silicon (c-Si) and amorphous Li_2Si (a-Li_2Si) were investigated. This two phase core-shell (c-Si as core and a-Li_2Si as shell) system forms at the beginning and evolves during the lithiation process in silicon nanowires. The lithiation process and the corresponding anisotropic swelling occurs through the non-uniform motion of the interfaces between a-Li_2Si and c-Si. It is found that Li is initially adsorbed on the (110) surface of c-Si and its diffusion energy barrier on the fully covered (110) surface is less than that of (111) and (100) surfaces. Due to the amorphous nature of the Li_2Si phase, a range of values was obtained for the diffusion energy barriers corresponding to the incorporation of Li from a-Li_2Si into c-Si, i.e. at the interfaces of the core/shell system. Results showed that the interface formation energy of a-Li_2Si|c-Si(110) is less favorable than a-Li_2Si|c-Si(111) and a-Li_2Si|c-Si(100) interfaces. Therefore, it is concluded that the experimentally-observed anisotropic swelling of silicon nanowires during the lithiation process is governed by thermodynamic factor, i.e various interface formation energies, which are orientation dependent. In this study, it was shown that the contribution of the 3D Li diffusion (kinetic) to the growth process

is minimal.

In the publication **A2**, the stability of all possible types of defects in Li_2S was evaluated in both charged and neutral states by plotting the calculated defect formation energies as function of the chemical potential of Li (cell voltage). It was shown that for a wide range of cell voltages, Frenkel pair (combination of charged lithium vacancy and interstitial lithium) with the lowest defect formation energy is the most stable defect type. In the next step, the diffusion energy barriers for single vacancy, divacancy and interstitial knock-off mechanisms were calculated. It was found that the migration of a single Li vacancy is the most favorable diffusion mechanism in bulk Li_2S. As a result, formation and migration of single Li vacancies are responsible for the ionic conductivity of Li_2S. The large activation energy obtained in this study explains the reason behind low ionic conductivity of Li_2S and confirms the experimentally-observed hindering of further lithiation of sulfur due to the formation of Li_2S in Li-S batteries. Since the formation energies of vacancy and interstitial defects in Li_2S are almost the same, due to the lower migration energy of single Li vacancy hopping, kinetic is the dominant factor in determining the conductivity.

In the publications **A3, A4 and A5**, 2D Li diffusion in bulk and $(10\bar{1}4)$ surface as well as polaron hopping in bulk of $LiCoO_2$ were studied. Moreover, the effect of strain as an important factor to manipulate the conductivity in bulk $LiCoO_2$ was explored using the elastic dipole tensor method. First it was shown that the ionic diffusion energy barrier is independent of the spin polarization of the system. In addition, it was demonstrated that the curved migration pathway of the Li diffusion into a divacancy of Li which is valid for the bulk can be detected on the $(10\bar{1}4)$ surface as well. It was revealed that the energy barrier for this mechanism on the topmost layer of the $(10\bar{1}4)$ surface is almost zero. Furthermore, for both bulk and $(10\bar{1}4)$ surface, it was found that PBE+U XC functional for Li vacancy migration calculations presents contributions of both ionic and polaronic diffusion energy barriers while with PBE functional only the ionic migration energy was obtained. This last finding was a motivation to further study the electronic conductivity in bulk $LiCoO_2$ using small-polaron hopping mechanism. In order to evaluate the effect of stress/strain on conductivity, the concept of elastic dipole tensor was introduced. The aim was to prove that this concept can be used to analytically predict the behavior of strained system with much less computational efforts. As a result, for a specific defect concentration, elastic dipole tensor was calculated and then formation and migration energies of single Li vacancy in $LiCoO_2$ as a function of strain was evaluated. It was shown that this approach is in a good agreement with the computationally-demanding

direct method in which formation and migration energies were calculated at each strain regime. Moreover, it was revealed that even a small amount of strain in bulk $LiCoO_2$ can change the activation energy and hence the ionic conductivity up to one order of magnitude (depending on the type of strain) which is also in agreement with experimental observations. Finally, using the concept of self-trapped small polarons and NEB calculations, the energy barrier of polaron hopping and electronic conductivity in bulk $LiCoO_2$ were estimated. It was demonstrated that the effect of strain on the electronic conductivity can also be predicted using the elastic dipole tensor method. This effect on electronic conductivity is less pronounced than the ionic one. Using the elastic dipole method, it is possible to achieve a much higher efficiency in the investigation of the effect of complicated and multi-component strain fields on charge carriers mobilities.

Ab initio-based calculations of conductivity in selected battery materials revealed that thermodynamic and kinetic factors can be unevenly decisive. Therefore, in order to manipulate the conductivity in battery materials, the first step is to find the dominant factor and then for example by changing the stress/strain or concentration of defects, conductivity and hence performance of a battery system can be engineered. These approaches can be used to study similar systems. As the future studies, using our knowledge from the first and second sections of the results chapter, in similar systems with two phase reaction mechanisms, the interface between the two phases can be modeled and investigated. Moreover, the interfaces between electrodes and electrolyte (specially solid electrolytes), which are very important in the charging/discharging processes and are determining in the performance of battery systems, can be explored. In addition, effect of strain in the solid electrolytes and at the mentioned interfaces between electrode and electrolytes can be studied using the elastic dipole tensor approach. As an extension to the third section of the results chapter, investigation of the effect of strain on conductivity together with the coupling between the polaronic and ionic defects and high defects concentration can be studied in the future.

Acknowledgement

First and foremost, I would like to thank my supervisor, Dr. Payam Kaghazchi, who introduced me to the world of quantum mechanical modeling in electrochemistry and taught me a lot in this field.

I am greatly thankful to Prof. Beate Paulus at Freie Universität Berlin for her priceless comments on my thesis and her enormous help throughout my doctoral studies.

I also would like to thank Prof. Karsten Albe at Technische Universität Darmstadt for his brilliant ideas and fruitful discussions. He kindly provided me with the required facilities to conduct my research at TUD.

I am keenly grateful to Dr. Jochen Rohrer at Technische Universität Darmstadt for his great notions.

Many thanks to my colleagues and friends at Freie Universität Berlin (Sara, Melissa, Qian and Pouya) and Technische Universität Darmstadt (Kai, Daniel, Conny, Markus and Marcel).

Special thanks to the administrators of computer clusters at Freie Universität Berlin (Dr. Loris Bennett) and Technische Universität Darmstadt (Thomas Opfer).

My great appreciation goes to my loving parents and my uncle Behruz for all their selfless help and support during my life and education.

Last but not least, I express my deepest gratitude to my amazing and wonderful wife, Sareh, who has always stood by my side all these years. Without her, this was not possible.

Declaration of Authorship

I hereby confirm that I have authored this doctorate thesis independently and without use of others than the indicated sources. All passages which are literally or in general matter taken out of publications or other sources are cited as such.

Berlin, 04.12.2017

Ashkan Moradabadi

References

[1] C. Lefrou, P. Fabry, and J. C. Poignet. *Electrochemistry*. Springer Nature, 2012.

[2] H. Chen *et al.* "Progress in electrical energy storage system: A critical review". *Progress in Natural Science* 19.3 (2009), pp. 291–312.

[3] M. Park *et al.* "A review of conduction phenomena in Li-ion batteries". *Journal of Power Sources* 195.24 (2010), pp. 7904–7929.

[4] P. Heitjans and J. Kärger. *Diffusion in Condensed Matter: Methods, Materials, Models*. SpringerLink: Springer e-Books. Springer Berlin Heidelberg, 2006.

[5] M. Pollak and B. Shklovskii. *Hopping Transport in Solids*. Modern Problems in Condensed Matter Sciences. Elsevier Science, 1991.

[6] D. Emin. *Polarons*. Cambridge University Press, 2012.

[7] K. Ozawa. "Lithium-ion rechargeable batteries with $LiCoO_2$ and carbon electrodes: the $LiCoO_2$/C system". *Solid State Ionics* 69.3-4 (1994), pp. 212–221.

[8] J. M. Tarascon and M. Armand. "Issues and challenges facing rechargeable lithium batteries". *Nature* 414.6861 (2001), pp. 359–367.

[9] M. R. Palacín. "Recent advances in rechargeable battery materials: A chemist's perspective". *Chemical Society Reviews* 38.9 (2009), p. 2565.

[10] X. Ji and L. F. Nazar. "Advances in Li–S batteries". *Journal of Materials Chemistry* 20.44 (2010), p. 9821.

[11] V. Etacheri *et al.* "Challenges in the development of advanced Li-ion batteries: A review". *Energy & Environmental Science* 4.9 (2011), p. 3243.

[12] D. Aurbach. "Review of selected electrode–solution interactions which determine the performance of Li and Li ion batteries". *Journal of Power Sources* 89.2 (2000), pp. 206–218.

[13] D. Deng. "Li-ion batteries: basics, progress, and challenges". *Energy Science & Engineering* 3.5 (2015), pp. 385–418.

[14] P. Verma, P. Maire, and P. Novák. "A review of the features and analyses of the solid electrolyte interphase in Li-ion batteries". *Electrochimica Acta* 55.22 (2010), pp. 6332–6341.

[15] K. Edström, T. Gustafsson, and J. Thomas. "The cathode–electrolyte interface in the Li-ion battery". *Electrochimica Acta* 50.2-3 (2004), pp. 397–403.

[16] P. G. Bruce *et al.* "Li–O_2 and Li–S batteries with high energy storage". *Nature Materials* 11.1 (2011), pp. 19–29.

[17] Y. X. Yin *et al.* "Lithium-Sulfur Batteries: Electrochemistry, Materials, and Prospects". *Angewandte Chemie International Edition* 52.50 (2013), pp. 13186–13200.

[18] Y. Yang *et al.* "New nanostructured Li_2S/silicon rechargeable battery with high specific energy". *Nano Letters* 10.4 (2010), pp. 1486–1491.

[19] R. Xu *et al.* "Insight into sulfur reactions in Li–S batteries". *ACS Applied Materials & Interfaces* 6.24 (2014), pp. 21938–21945.

[20] Y. Yang, G. Zheng, and Y. Cui. "Nanostructured sulfur cathodes". *Chemical Society Reviews* 42.7 (2013), p. 3018.

[21] K. Cai *et al.* "Nanostructured Li_2S–C composites as cathode material for high-energy lithium/sulfur batteries". *Nano Letters* 12.12 (2012), pp. 6474–6479.

[22] A. Moradabadi and P. Kaghazchi. "Thermodynamics and kinetics of defects in Li_2S". *Applied Physics Letters* 108.21 (2016), p. 213906.

[23] J. Rohrer and K. Albe. "Insights into degradation of Si anodes from first-principle calculations". *The Journal of Physical Chemistry C* 117.37 (2013), pp. 18796–18803.

[24] A. Moradabadi and P. Kaghazchi. "Mechanism of Li intercalation/deintercalation into/from the surface of $LiCoO_2$". *Phys. Chem. Chem. Phys.* 17.35 (2015), pp. 22917–22922.

[25] P. Trucano and R. Chen. "Structure of graphite by neutron diffraction". *Nature* 258.5531 (1975), pp. 136–137.

[26] S. W. Lee *et al.* "Anomalous shape changes of silicon nanopillars by electrochemical lithiation". *Nano Letters* 11.7 (2011), pp. 3034–3039.

[27] M. Endo *et al.* "Recent development of carbon materials for Li ion batteries". *Carbon* 38.2 (2000), pp. 183–197.

[28] E. Yoo *et al.* "Large reversible Li storage of graphene nanosheet families for use in rechargeable lithium ion batteries". *Nano Letters* 8.8 (2008), pp. 2277–2282.

[29] N. Nitta *et al.* "Li-ion battery materials: present and future". *Materials Today* 18.5 (2015), pp. 252–264.

[30] C. K. Chan *et al.* "High-performance lithium battery anodes using silicon nanowires". *Nature Nanotechnology* 3.1 (2007), pp. 31–35.

[31] W. Wang and P. N. Kumta. “Reversible high capacity nanocomposite anodes of Si/C/SWNTs for rechargeable Li-ion batteries”. *Journal of Power Sources* 172.2 (2007), pp. 650–658.

[32] L. F. Cui *et al.* “Carbon-silicon core-shell nanowires as high capacity electrode for lithium ion batteries”. *Nano Letters* 9.9 (2009), pp. 3370–3374.

[33] H. Yang *et al.* “Orientation-dependent interfacial mobility governs the anisotropic swelling in lithiated silicon nanowires”. *Nano Letters* 12.4 (2012), pp. 1953–1958.

[34] X. H. Liu *et al.* “Anisotropic swelling and fracture of silicon nanowires during lithiation”. *Nano Letters* 11.8 (2011), pp. 3312–3318.

[35] J. Rohrer *et al.* “On the origin of anisotropic lithiation of silicon”. *Journal of Power Sources* 293 (2015), pp. 221–227.

[36] S. P. Jand, Q. Zhang, and P. Kaghazchi. “Theoretical study of superionic phase transition in Li_2S”. *Scientific Reports* 7.1 (2017).

[37] K. Mizushima *et al.* “Li_xCoO_2 ($0 \leq x \leq -1$): A new cathode material for batteries of high energy density”. *Materials Research Bulletin* 15.6 (1980), pp. 783–789.

[38] R Koksbang. “Cathode materials for lithium rocking chair batteries”. *Solid State Ionics* 84.1-2 (1996), pp. 1–21.

[39] M. Okubo *et al.* “Nanosize effect on high-rate Li-ion intercalation in $LiCoO_2$ electrode”. *Journal of the American Chemical Society* 129.23 (2007), pp. 7444–7452.

[40] Y. Sun, S. E. Thompson, and T. Nishida. “Physics of strain effects in semiconductors and metal-oxide-semiconductor field-effect transistors”. *Journal of Applied Physics* 101.10 (2007), p. 104503.

[41] E. Penev, P. Kratzer, and M. Scheffler. “Effect of strain on surface diffusion in semiconductor heteroepitaxy”. *Physical Review B* 64.8 (2001).

[42] J. Zhu, F. Liu, and M. A. Scarpulla. “Strain tuning of native defect populations: The case of $Cu_2ZnSn(S, Se)_4$”. *APL Materials* 2.1 (2014), p. 012110.

[43] X. Li *et al.* “Strain effects on the thermal conductivity of nanostructures”. *Physical Review B* 81.24 (2010).

[44] A. Barai *et al.* “A study of the effects of external pressure on the electrical performance of a lithium-ion pouch cell”. *2013 International Conference on Connected Vehicles and Expo (ICCVE)*. Institute of Electrical and Electronics Engineers (IEEE), 2013.

[45] J. Cannarella and C. B. Arnold. “Stress evolution and capacity fade in constrained lithium-ion pouch cells”. *Journal of Power Sources* 245 (2014), pp. 745–751.

[46] J. Gnanaraj *et al.* “The effect of pressure on the electroanalytical response of graphite anodes and $LiCoO_2$ cathodes for Li-ion batteries”. *Journal of Electroanalytical Chemistry* 516.1-2 (2001), pp. 89–102.

[47] T. Zhang and Z. Guo. “Effects of electrode properties and fabricated pressure on Li ion diffusion and diffusion-induced stresses in cylindrical Li-ion batteries”. *Modelling and Simulation in Materials Science and Engineering* 22.2 (2014), p. 025016.

[48] A. Moradabadi *et al.* “Influence of elastic strain on the thermodynamics and kinetics of lithium vacancy in bulk-$LiCoO_2$”. *arXiv preprint arXiv:1706.01709* (2017).

[49] A. J. E. Rettie *et al.* “Unravelling small-polaron transport in metal oxide photoelectrodes”. *The Journal of Physical Chemistry Letters* 7.3 (2016), pp. 471–479.

[50] A. M. Stoneham *et al.* “Trapping, self-trapping and the polaron family”. *Journal of Physics: Condensed Matter* 19.25 (2007), p. 255208.

[51] A. Moradabadi and P. Kaghazchi. “Effect of strain on polaron hopping and electronic conductivity in bulk $LiCoO_2$”. *Physical Review Applied* 7.6 (2017).

[52] P. Hohenberg and W. Kohn. “Inhomogeneous electron gas”. *Physical Review* 136.3B (1964), pp. 864–871.

[53] W. Kohn and L. J. Sham. “Self-consistent equations including exchange and correlation effects”. *Physical Review* 140.4A (1965), pp. 1133–1138.

[54] E. Schrödinger. “Quantisierung als Eigenwertproblem”. *Annalen der Physik* 384.4 (1926), pp. 361–376.

[55] M. Longair. *Quantum Concepts in Physics: An Alternative Approach to the Understanding of Quantum Mechanics*. Cambridge University Press, 2013.

[56] M. Born and R. Oppenheimer. “Zur Quantentheorie der Molekeln”. *Annalen der Physik* 389.20 (1927), pp. 457–484.

[57] D. R. Hartree. “The wave mechanics of an atom with a non-Coulomb central field. Part I. Theory and methods”. *Mathematical Proceedings of the Cambridge Philosophical Society*. Vol. 24. 01. Cambridge Univ Press. 1928, pp. 89–110.

[58] J. C. Slater. “The theory of complex spectra”. *Physical Review* 34.10 (1929), pp. 1293–1322.

[59] V. Fock. “Näherungsmethode zur Lösung des quantenmechanischen Mehrkörperproblems”. *Zeitschrift für Physik* 61.1-2 (1930), pp. 126–148.

[60] D. Hartree and W. Hartree. “Self-consistent field, with exchange, for beryllium”. *Proceedings of the Royal Society of London. Series A, Mathematical and Physical Sciences* 150.869 (1935), pp. 9–33.

[61] C. D. Sherrill and H. F. Schaefer. “The configuration interaction method: Advances in highly correlated approaches”. *Advances in Quantum Chemistry*. Elsevier, 1999, pp. 143–269.

[62] H. J. Monkhorst. “Calculation of properties with the coupled-cluster method”. *International Journal of Quantum Chemistry* 12.S11 (2009), pp. 421–432.

[63] W. Tobocman. “Many-body perturbation theory”. *Physical Review* 107.1 (1957), pp. 203–208.

[64] R. J. Bartlett and J. F. Stanton. “Applications of post-Hartree—Fock methods: A tutorial”. *Reviews in Computational Chemistry*. John Wiley & Sons, Inc., pp. 65–169.

[65] V. Magnasco. *Methods of molecular quantum mechanics: An introduction to electronic molecular structure*. John Wiley & Sons, Ltd, 2009, pp. 133–139.

[66] L. H. Thomas. “The calculation of atomic fields”. *Mathematical proceedings of the Cambridge philosophical society*. Vol. 23. 05. Cambridge Univ Press. 1927, pp. 542–548.

[67] E. Fermi. “Eine statistische Methode zur Bestimmung einiger Eigenschaften des Atoms und ihre Anwendung auf die Theorie des periodischen Systems der Elemente”. *Zeitschrift für Physik* 48.1-2 (1928), pp. 73–79.

[68] S. H. Vosko, L. Wilk, and M. Nusair. “Accurate spin-dependent electron liquid correlation energies for local spin density calculations: a critical analysis”. *Canadian Journal of Physics* 58.8 (1980), pp. 1200–1211.

[69] P. A. M. Dirac. “Note on exchange phenomena in the Thomas atom”. *Mathematical proceedings of the Cambridge philosophical society* 26.03 (1930), p. 376.

[70] D. M. Ceperley and B. J. Alder. “Ground state of the electron gas by a stochastic method”. *Physical Review Letters* 45.7 (1980), pp. 566–569.

[71] J. P. Perdew and Y. Wang. “Accurate and simple analytic representation of the electron-gas correlation energy”. *Physical Review B* 45.23 (1992), pp. 13244–13249.

[72] C. Stampfl and C. G. V. de Walle. “Density-functional calculations for III-V nitrides using the local-density approximation and the generalized gradient approximation”. *Physical Review B* 59.8 (1999), pp. 5521–5535.

[73] A. van de Walle and G. Ceder. “Correcting overbinding in local-density-approximation calculations”. *Physical Review B* 59.23 (1999), pp. 14992–15001.

[74] J. P. Perdew *et al.* “Atoms, molecules, solids, and surfaces: Applications of the generalized gradient approximation for exchange and correlation”. *Physical Review B* 46.11 (1992), pp. 6671–6687.

[75] J. P. Perdew, K. Burke, and M. Ernzerhof. “Generalized gradient approximation made simple”. *Physical Review Letters* 77.18 (1996), pp. 3865–3868.

[76] J. P. Perdew. “Density functional theory and the band gap problem”. *International Journal of Quantum Chemistry* 28.S19 (2009), pp. 497–523.

[77] V. I. Anisimov, J. Zaanen, and O. K. Andersen. “Band theory and Mott insulators: HubbardUinstead of StonerI”. *Physical Review B* 44.3 (1991), pp. 943–954.

[78] G. Kotliar *et al.* “Electronic structure calculations with dynamical mean-field theory”. *Reviews of Modern Physics* 78.3 (2006), pp. 865–951.

[79] S. Sharma *et al.* “Reduced density matrix functional for many-electron systems”. *Physical Review B* 78.20 (2008).

[80] V. I. Anisimov *et al.* “Density-functional theory and NiO photoemission spectra”. *Physical Review B* 48.23 (1993), pp. 16929–16934.

[81] B. Himmetoglu *et al.* “Hubbard-corrected DFT energy functionals: The LDA+U description of correlated systems”. *International Journal of Quantum Chemistry* 114.1 (2013), pp. 14–49.

[82] S. L. Dudarev *et al.* “Electron-energy-loss spectra and the structural stability of nickel oxide: An LSDA+U study”. *Physical Review B* 57.3 (1998), pp. 1505–1509.

[83] http://dft.sandia.gov/Quest/.

[84] G. Kresse and J. Furthmüller. “Efficient iterative schemes for ab initio total-energy calculations using a plane-wave basis set”. *Physical Review B* 54.16 (1996), pp. 11169–11186.

[85] R. Dovesi *et al.* “Ab initio quantum simulation in solid state chemistry”. *Reviews in computational chemistry* 21 (2005), p. 1.

[86] F. Bloch. “Über die quantenmechanik der elektronen in kristallgittern”. *Zeitschrift für Physik A Hadrons and Nuclei* 52.7 (1929), pp. 555–600.

[87] H. J. Monkhorst and J. D. Pack. “Special points for Brillouin-zone integrations”. *Physical Review B* 13.12 (1976), pp. 5188–5192.

[88] U. von Barth and C. D. Gelatt. “Validity of the frozen-core approximation and pseudopotential theory for cohesive energy calculations”. *Physical Review B* 21.6 (1980), pp. 2222–2228.

[89] D. R. Hamann, M. Schlüter, and C. Chiang. “Norm-conserving pseudopotentials”. *Physical Review Letters* 43.20 (1979), pp. 1494–1497.

[90] P. E. Blöchl. “Projector augmented-wave method”. *Physical Review B* 50.24 (1994), pp. 17953–17979.

[91] I. N. Levine. *Quantum Chemistry, Volume 1*. Pearson Education, 2009.

[92] W. Koch and M. C. Holthausen. *A Chemist's Guide to Density Functional Theory, 2nd Edition*. Wiley-VCH, 2001.

[93] P. G. Bruce. *Solid state electrochemistry*. Vol. 5. Cambridge University Press, 1997.

[94] S. Zhang and J. Northrup. “Chemical potential dependence of defect formation energies in GaAs: Application to Ga self-diffusion”. *Physical Review Letters* 67.17 (1991), pp. 2339–2342.

[95] C. Freysoldt *et al.* “First-principles calculations for point defects in solids”. *Reviews of Modern Physics* 86.1 (2014), pp. 253–305.

[96] H. Jónsson, G. Mills, and K. W. Jacobsen. “Nudged elastic band method for finding minimum energy paths of transitions” (1998).

[97] G. Henkelman, B. P. Uberuaga, and H. Jónsson. “A climbing image nudged elastic band method for finding saddle points and minimum energy paths”. *The Journal of Chemical Physics* 113.22 (2000), pp. 9901–9904.

[98] J. D. S. Donald A. McQuarrie. *Physical chemistry: A molecular approach*. University Science Books, 1997.

[99] C. Freysoldt, J. Neugebauer, and C. G. V. de Walle. “Fully *ab initio* finite-size corrections for charged-defect supercell calculations”. *Physical Review Letters* 102.1 (2009).

[100] C. Freysoldt, J. Neugebauer, and C. G. V. de Walle. “Electrostatic interactions between charged defects in supercells”. *physica status solidi (b)* 248.5 (2010), pp. 1067–1076.

[101] H. P. Komsa, T. T. Rantala, and A. Pasquarello. “Finite-size supercell correction schemes for charged defect calculations”. *Physical Review B* 86.4 (2012).

[102] URL:https://www.mathworks.com/matlabcentral/fileexchange.

[103] *Computational Chemistry*. Springer US, Kluwer Academic Publishers, 2004.

[104] G. Henkelman. “Methods for Calculating Rates of Transitions with Application to Catalysis and Crystal Growth”. Doctoral Dissertation. University of Washington, 2001.

[105] P. Pechukas. “Transition state theory”. *Annual Review of Physical Chemistry* 32.1 (1981), pp. 159–177.

[106] B. J. G. James M. Gere. *Mechanics of Materials*. Cengage Learning, 2008.

[107] P. Haupt. *Continuum Mechanics and Theory of Materials Advanced texts in physics*. Springer, 2000.

[108] W. D. Means. “Strain fields”. *Stress and Strain*. Springer New York, 1976, pp. 215–223.

[109] M. J. Gillan. “The long-range distortion caused by point defects”. *Philosophical Magazine A* 48.6 (1983), pp. 903–919.

[110] M. J. Gillan. “The elastic dipole tensor for point defects in ionic crystals”. *Journal of Physics C: Solid State Physics* 17.9 (1984), pp. 1473–1488.

[111] M Leslie and N. J. Gillan. “The energy and elastic dipole tensor of defects in ionic crystals calculated by the supercell method”. *Journal of Physics C: Solid State Physics* 18.5 (1985), pp. 973–982.

[112] D. A. Freedman, D. Roundy, and T. A. Arias. “Elastic effects of vacancies in strontium titanate: Short- and long-range strain fields, elastic dipole tensors, and chemical strain”. *Physical Review B* 80.6 (2009), p. 064108.

[113] P. Drude. “Zur Elektronentheorie der Metalle”. *Annalen der Physik* 306.3 (1900), pp. 566–613.

[114] B. Yacobi. *Semiconductor Materials: An Introduction to Basic Principles (Microdevices)*. Springer, 2003.

[115] R. A. Marcus. “Chemical and electrochemical electron-transfer theory”. *Annual Review of Physical Chemistry* 15.1 (1964), pp. 155–196.

[116] URL:http://www.ch.ic.ac.uk.

[117] A. L. Shluger and A. M. Stoneham. “Small polarons in real crystals: concepts and problems”. *Journal of Physics: Condensed Matter* 5.19 (1993), pp. 3049–3086.

[118] S. C. Jung and Y.-K. Han. “Facet-dependent lithium intercalation into Si crystals: Si(100) vs. Si(111)”. *Physical Chemistry Chemical Physics* 13.48 (2011), p. 21282.

[119] P. Kaghazchi. “Mechanism of Li intercalation into Si”. *Applied Physics Letters* 102.9 (2013), p. 093901.

[120] G. A. Tritsaris *et al.* “Diffusion of lithium in bulk amorphous silicon: A theoretical study”. *The Journal of Physical Chemistry C* 116.42 (2012), pp. 22212–22216.

[121] V. L. Chevrier and J. R. Dahn. “First principles model of amorphous silicon lithiation”. *Journal of The Electrochemical Society* 156.6 (2009), A454.

[122] H. Kim *et al.* “Structure and properties of Li-Si alloys: A first-principles study”. *The Journal of Physical Chemistry C* 115.5 (2011), pp. 2514–2521.

[123] T. L. Chan and J. R. Chelikowsky. “Controlling diffusion of lithium in silicon nanostructures”. *Nano Letters* 10.3 (2010), pp. 821–825.

[124] Q. Zhang *et al.* “Lithium insertion In silicon nanowires: An *ab initio* study”. *Nano Letters* 10.9 (2010), pp. 3243–3249.

[125] M. K. Y. Chan, C. Wolverton, and J. P. Greeley. “First principles simulations of the electrochemical lithiation and delithiation of faceted crystalline silicon”. *Journal of the American Chemical Society* 134.35 (2012), pp. 14362–14374.

[126] A. V. der Ven *et al.* “First-principles investigation of phase stability in Li_xCoO_2”. *Physical Review B* 58.6 (1998), pp. 2975–2987.

[127] D. Kramer and G. Ceder. “Tailoring the morphology of $LiCoO_2$: A first principles study”. *Chemistry of Materials* 21.16 (2009), pp. 3799–3809.

[128] A. V. der Ven and G. Ceder. “Lithium diffusion mechanisms in layered intercalation compounds”. *Journal of Power Sources* 97-98 (2001), pp. 529–531.

[129] H. Xia, L. Lu, and G. Ceder. “Li diffusion in $LiCoO_2$ thin films prepared by pulsed laser deposition”. *Journal of Power Sources* 159.2 (2006), pp. 1422–1427.

[130] F. Ning *et al.* "Strain tuned Li diffusion in $LiCoO_2$ material for Li ion batteries: A first principles study". *Solid State Ionics* 263 (2014), pp. 46–48.

[131] X.-Y. Qiu *et al.* "Electrochemical and electronic properties of $LiCoO_2$ cathode investigated by galvanostatic cycling and EIS". *Physical Chemistry Chemical Physics* 14.8 (2012), p. 2617.

[132] S. Levasseur, M. Ménétrier, and C. Delmas. "On the dual effect of Mg doping in $LiCoO_2$ and $Li_{1+\delta}CoO_2$: Structural, electronic properties, and ^{7}Li MAS NMR studies". *Chemistry of Materials* 14.8 (2002), pp. 3584–3590.